Journal of Sedimentary Research

Journal of Sedimentary Research, 2022, v. 92, 32–49
Research Article
DOI: 10.2110/jsr.2021.018

THE LATE MIOCENE EOLIAN RECORD AT THE EASTERN MARGIN OF THE PUNA PLATEAU, NW ARGENTINA: EVIDENCE OF UPPER-TROPOSPHERIC PALEOCIRCULATION

JONATHAN LEDESMA,[1] CECILIA E. DEL PAPA,[1] AND PATRICIO PAYROLA[2]

[1]*Centro de Investigaciones en Ciencias de la Tierra (CICTERRA), CONICET, Universidad Nacional de Córdoba, Avenida Vélez Sarsfield 1611, X5016GCA Córdoba, Argentina*

[2]*Instituto de Bio y Geociencias del NOA (IBIGEO), CONICET, Universidad Nacional de Salta, Avenida 10 Bolivia 5150, 4400 Salta, Argentina*

e-mail: jonathanledesma@unc.edu.ar

ABSTRACT: **The Puna–Altiplano Plateau of the Central Andes is the second-highest plateau in the world (after Tibet), with a mean elevation of 4000 m.a.s.l. and an arid to hyperarid climate. Uplift of the Puna–Altiplano Plateau has affected lower-level atmospheric circulation, acting as a barrier to humid easterly winds from the Amazon basin and favoring an across-strike precipitation gradient resulting in a humid climate towards the east of the plateau and an arid to hyperarid climate in the orogen's interior. In the modern climate, the Bolivian High anticyclone regulates upper troposphere circulation, but little is known about the high-altitude tropospheric circulation of the past. This work focuses on the eolian record of the San Antonio de los Cobres basin along the eastern border of the Puna Plateau, NW Argentina, with the aim of analyzing its origin and thus elucidating the late Miocene winds. The eolian deposits are constrained by 7.8 Ma (K/Ar and U/Pb) and 6.4 Ma (U/Pb) ignimbrites at the nearly basal and upper contacts, respectively. Based on stratigraphic, sedimentological, and provenance analysis of the eolian units, we have identified three main facies associations (FAs): FA1) cross-stratified sandstones with large- to small-scale tabular, planar cross-bedding and with trough cross-stratification; FA2) sandstones with planar to low-angle stratification associated with thinly laminated ripple sandstone strata; FA3) medium- to coarse-grained massive sandstones associated with pebbly to bouldery, matrix-supported conglomerates and clast-supported conglomerates. The lateral and vertical facies assemblages indicate a dune field confined to topographic depressions dominated by transverse dunes with straight and sinuous crestlines that laterally grade into sandsheets associated with ephemeral streams. Paleoflows, lithotypes, and grain-size determinations indicate a persistent north-northwest provenance and wind velocities of 24–38 km/h (with maximum velocities of 55–75 km/h).**

The results of our analysis coupled with data from previous studies indicates that, for at least the last ca. 8 Myr, the winds have been blowing constantly from the north-northwest with an intensity similar to the present. This implies that the paleo-atmospheric circulation had a similar pattern to the present-day one. Therefore, we conclude that the upper-troposphere circulation in the Puna Plateau of NW Argentina was already regulated by the Bolivian High anticyclone during the Miocene, generating constant north-northwesterly winds.

INTRODUCTION

The Argentine Puna Plateau is an orogenic region between 22° and 27° S with an average elevation of 3700 m.a.s.l. that, along with the Bolivian Altiplano, forms the second-highest plateau in the world (Fig. 1A, B). This region stretches for ~ 2000 km along the Central Andes, from southern Peru to northwestern Argentina, and ranges between 350 and 400 km in width (Fig. 1B) (Isacks 1988; Allmendinger et al. 1997). This plateau is the result of orogenic growth in response to the subduction of the Nazca Plate beneath the South American Plate (Allmendinger et al. 1983; Isacks 1988).

Current discussions concerning the origin, topographic growth, and evolution of the high-elevation Puna Plateau include its impact on aridification related to Miocene atmospheric circulation (Hartley 2003; Vera et al. 2006; Strecker et al. 2007; Pingel et al. 2016; Rohrmann et al. 2016; among others). Numerous studies postulate that the uplift of the Puna Plateau from the late Oligocene to early Miocene acted as a variable favoring the arid to hyperarid climate regime recorded in the sediments as closed evaporitic and isolated basins (e.g., Vandervoort et al. 1995; Hartley 2003; Lamb and Davis 2003; Sobel et al. 2003; Ehlers and Poulsen 2009; Armijo et al. 2015). Although a more humid climate predominates on the eastern flank of the Puna Plateau, with mean annual precipitation ranging between 600 and more than 2000 mm/year in the Eastern Cordillera and Subandean Ranges, the interior of the Puna Plateau is arid to hyperarid (Bianchi et al. 2005; Strecker et al. 2007; Pingel et al. 2016). In this regard, the analysis of eolian and evaporitic sedimentary records and distributions could be key to understanding the scenarios in which these events occurred.

Topographic growth of the Central Andes orogen has influenced present-day low-level atmospheric circulation and moisture-transport patterns in South America by acting as an orographic barrier intercepting lower-level (850 hPa) moisture-bearing easterly winds (Fig. 1A) (e.g., Vera et al. 2006; Garreaud and Aceituno 2007; Strecker et al. 2007; Garreaud et al. 2010; Poulsen et al. 2010; Rohrmann et al. 2016; among others). On the

Published Online: January 2022
 1527-1404/22/092-32

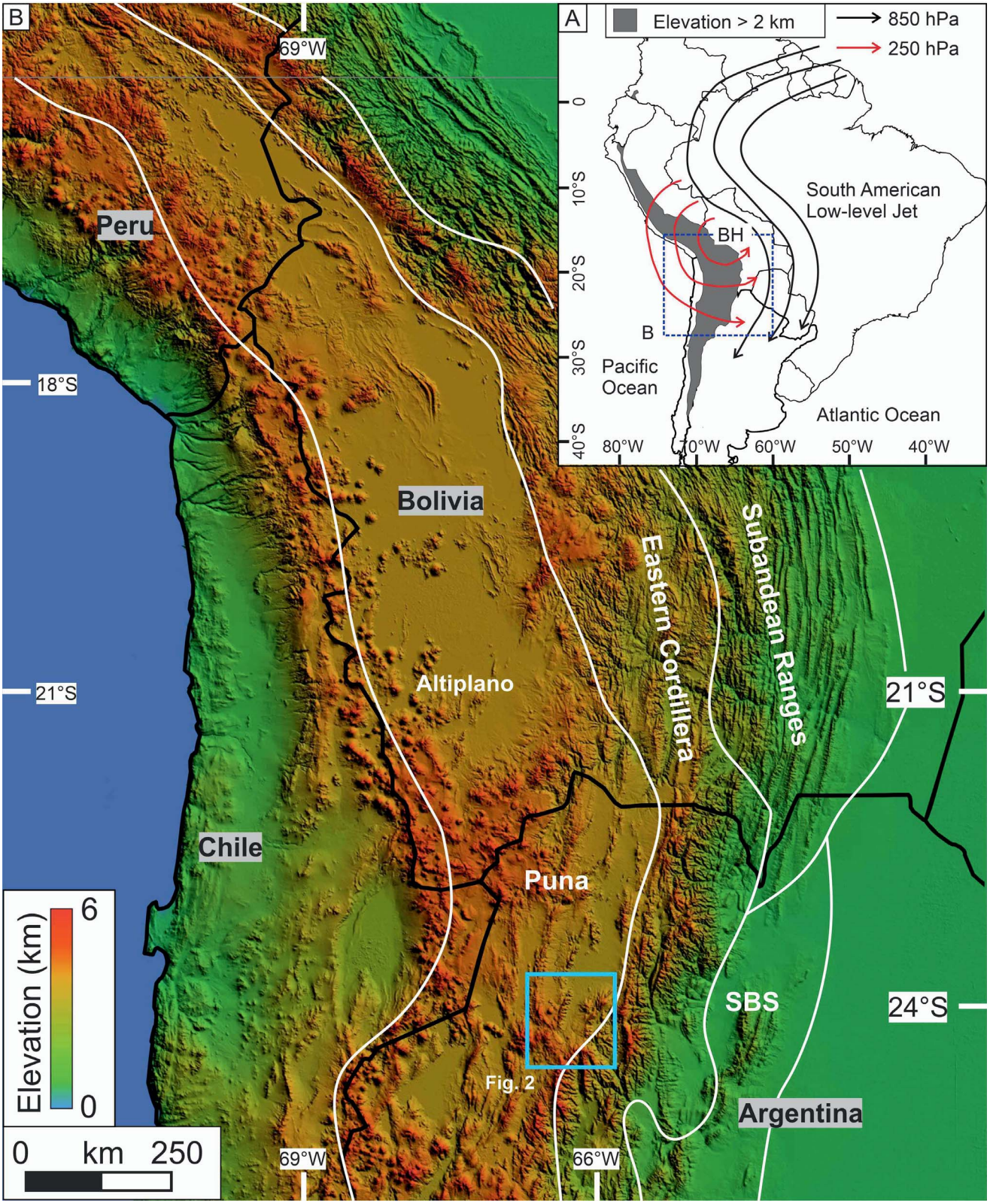

FIG. 1.—**A)** Large-scale circulation patterns in the South America summer-time (December, January, February) (after Lenters and Cook 1997; Vuille 1999; Vera et al. 2006; Fiorella et al. 2015; Pingel et al. 2016). BH, Bolivian High anticyclone. **B)** Digital elevation model (DEM) showing the distribution of heights in the Central Andes and the main geological provinces (after Strecker et al. 2007) SBS, Santa Barbara System.

other hand, the mid- to upper-level tropospheric circulation (250 hPa) is regulated by an anticyclone with its center over Bolivia and characterized by a strong seasonal behavior, called the Bolivian High (Fig. 1A, Gutman and Schwerdtfeger 1965; Virji 1981; Lenters and Cook 1997) which generates strong northwesterly winds over the Puna–Altiplano Plateau causing dry conditions (Garreaud et al. 2003). Little is known about the effects that the topographic uplift had on mid- to upper-level tropospheric circulation over the high-elevation Puna Plateau. Hartley (2003) proposed that the topographic growth of the Andes between 20 and 25°S by ca. 15 Ma favored arid conditions on the Puna–Altiplano Plateau.

The objective of this work is to provide new data on sandy eolian sedimentation in the Puna Plateau with the aim of analyzing its distribution and implications for mid- to high-altitude tropospheric circulation from the Miocene to the present. Our study is based on the sedimentological characteristics, paleocurrent indicators, regional distribution, and the correlation of the sandy eolian unit in the San Antonio de los Cobres basin with similar units along the Puna Plateau, NW Argentina. We found that the Miocene sandy eolian units along the eastern border of the Puna Plateau indicate predominant north-northwesterly paleowinds and calculated paleowind speeds similar to present-day ones, suggesting that the upper-troposphere circulation was already regulated by the Bolivian High anticyclone.

GEOLOGICAL SETTING

The Puna Plateau is characterized by low internal relief, closed and partially coalesced sedimentary basins, internal drainage, extensive volcanism, and an arid to hyperarid climate regime (Vandervoort et al. 1995; Sobel and Strecker 2003; Carrapa et al. 2005, 2009; Rohrmann et al. 2016; among others). East of the Puna Plateau, the Eastern Cordillera and Santa Bárbara System morphostructural provinces are characterized by north–south trending ranges decreasing in elevation to the east (Fig. 1B). The characteristic structural features of these provinces are basement-cored ranges limited by doubly vergent, high-angle reverse faults (Grier et al. 1991; Mon and Salfity 1995; Hongn and Seggiaro 2001; Kley and Monaldi 2002; Riller and Hongn 2003; Carrera et al. 2006). Uplifted basement blocks created a series of intermontane basins between the eastern margin of the Puna Plateau and the humid Andean foreland (Bookhagen and Strecker 2012).

This work focuses on a narrow belt of sandy eolian strata exposed in the intermontane San Antonio de los Cobres (SAC) basin, on the eastern border of the Puna Plateau (Figs. 1B, 2A, B). This basin is limited by regional reverse fault-related ranges striking approximately north–south (Fig. 2A). To the east, the basin is limited by the Muñano Range, formed by the west-vergent Muñano reverse fault which uplifts Precambrian and Ordovician rocks over Cenozoic rocks (Fig. 2A). To the west, the basin is limited by the Cobres Range, formed by the west-vergent Eastern Charco fault which carries Precambrian and Ordovician rocks over Cretaceous rocks through a high- to moderate-angle fault plane (Fig. 2A; del Papa and Petrinovic 2017). The SAC basin is limited to the south by the transtensional–transpressional Calama–Olcacapato–El Toro fault system (COT; Norini et al. 2013; Seggiaro et al. 2016; del Papa and Petrinovic 2017) and to the north by the Chimpa stratovolcano (Fig. 2A).

The oldest rocks in the area are represented by the Neo-Proterozoic Puncoviscana Formation. This unit largely crops out along the basin margins (Fig. 2A) and consists of a marine succession of sandstones, siltstones, and mudstones affected by low-grade metamorphism (Escayola et al. 2011; DoCampo et al. 2013). This unit is unconformably overlain by the Ordovician Parcha Formation, composed of marine sandstones, shales, and limestones (Harrington and Leanza 1957; Ramos 1973). The Cretaceous to early Eocene Salta Group overlies both Ordovician and Precambrian rocks, and corresponds to the filling of a rift basin (Fig. 2A; Salfity and Marquillas 1994). It is characterized by the conglomeratic Pirgua Subgroup, representing the synrift stage, and marine limestones and shales of the Balbuena Subgroup and fluvial sandstones and mudstones of the Santa Bárbara Subgroup, representing the postrift stage.

Middle Eocene to Pleistocene Andean foreland units are characterized mainly by coarse clastic sedimentation in alluvial-fan, fluvial, and fluvio-eolian environments. The stratigraphy is represented by the middle Eocene to Oligocene(?) Geste Formation, the middle Miocene Conglomerado Los Patos Formation, and the late Miocene to Pliocene(?) San Antonio de los Cobres Formation (Figs. 2B, 3, 4; del Papa and Petrinovic 2017; Pingel et al. 2019; Ledesma et al. 2019). The middle Miocene to Pleistocene sedimentary deposits are interbedded with volcanic units, mostly ignimbrites, such as the Vizcachayoc Ignimbrite, the Corte Blanco and Ramadas ignimbrites (Figs. 3, 4; Ledesma et al. 2019), and ignimbrites related to the Chimpa stratovolcano (Petrinovic et al. 1999, 2005; Riller et al. 2001; Arnosio et al. 2005; Ramelow et al. 2006; Arnosio 2010).

The eolian sediments that are the subject of this study are located in the late Miocene to Pliocene(?) San Antonio de los Cobres Formation (Pingel et al. 2019; Ledesma et al. 2019). This unit consists of two members: the lower eolian to fluvio-eolian Corte Blanco Member and the upper fluvial to alluvial Muñano Member (Fig. 3; Ledesma et al. 2019).

The Corte Blanco Member ranges between 50 to 110 m in thickness and consists mainly of thick sandstone packages intercalated with thin, medium to coarse conglomeratic strata interbedded with two ignimbrite beds. One ignimbrite bed is located near the base of the Member (the Corte Blanco Ignimbrite), and the other is located at the top of the Member (the Ramadas Ignimbrite) (Figs. 3, 4; Ledesma et al. 2019). The Corte Blanco Ignimbrite has two ages: 7.4 $\pm$ 0.3 Ma K-Ar biotite (Petrinovic et al. 1999) and 7.77 $\pm$ 0.06 Ma U-Pb zircon (Pingel et al. 2019). In turn, the upper Ramadas Ignimbrite has an age of 6.4 Ma U-Pb zircon (Pingel et al. 2019) and is widely distributed in the study area, making it a confident marker bed for stratigraphic correlations. These volcanic units constrain the age of the Corte Blanco Member to the late Miocene.

The Muñano Member is characterized by a coarsening-upward succession over $>$ 150 m thick composed of fine- to medium-grained sandstones interbedded with pebbly to cobbly conglomerates. These coarser deposits become more abundant towards the top, forming upward-thickening bodies of clast-supported, pebbly to bouldery conglomerates (Fig. 3; Ledesma et al. 2019). U-Pb zircon dating from a volcanic ash fall intercalated in the mid-stratigraphic section yielded an age of 5.49 $\pm$ 0.05 Ma (Pingel et al. 2019), so a late Miocene–Pliocene(?) age can be assigned to this member.

METHODOLOGY

To analyze the distribution and characteristics of the eolian deposits, they were mapped, logged, and sampled in five localities: 1) Corte Blanco, 2) Southern Los Patos Creek, 3) Northern Los Patos Creek, 4) Demise quarry, and 5) Piscuno (Figs. 2B, 4). Detailed bed-by-bed measurements, facies descriptions, and sampling were performed in each locality. Fieldwork consisted of the identification of sedimentary lithofacies (Table 1), lithofacies assemblages (facies associations), and 3D lithosome organization in architectural elements and key bounding surfaces according to Brookfield (1977) and Kocurek (1988).

The movement of sand grains and their organization in an eolian setting depends on the sand grain size and density, and wind direction and velocity (wind regime). Fluctuations in the wind regime will therefore be reflected in the internal structure of a sand dune and in its grain size. Recognition of these parameters is key for reconstructing the wind regime that built a sandy dune field (Pye and Tsoar 2009). To achieve this, the spatial arrangements of sedimentary structures, including reactivation surfaces and cross-bedding, were analyzed and measured in order to determine the predominant paleowind direction. Data were restored to horizontality; the Stereonet Software, version 10.0 (Richard W. Allmendinger, © 2018) was

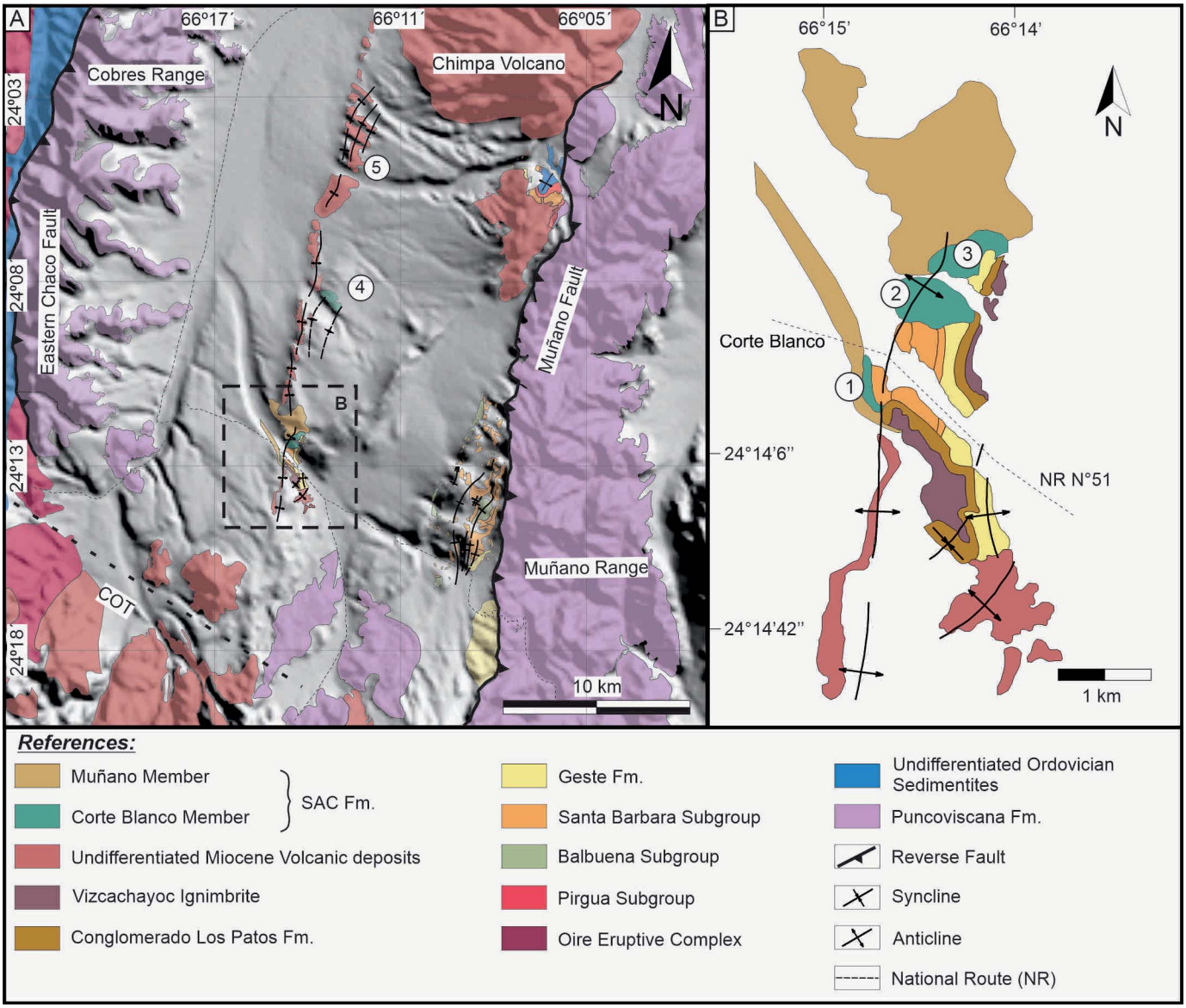

FIG. 2.—**A)** Geological map of the SAC Basin (modified from Blasco et al. 1996; Ledesma et al. 2019). **B)** Geological map of the study area showing the distribution of the San Antonio de los Cobres Formation and its relationship with the outcropping units in the basin (modified from del Papa and Petrinovic 2017; Ledesma et al. 2019).

used for calculations (Allmendinger et al. 2012). Rose diagrams were plotted in the upper hemisphere (Potter and Pettijohn 1977).

The sampling method focused on facies variations along the outcrops. Samples of at least 150 grams were collected. Sample preparation for textural analysis consisted of treatment with hydrochloric acid and hydrogen peroxide to remove the cement and organic matter, respectively. Once the cement had been removed, the samples were separated into aliquots of 100 grams and subsequently sieved for 15 minutes in a semiautomatic, motor-driven mechanical sieve shaker using a set of standard ASTM sieves. Sediment weight retained on each mesh was recalculated to a percentage. The textural analysis of grain sizes, the distribution, and statistics were performed using the GRADISTAT statistical package (Blott and Pye 2001) presented in Table 2. Statistical parameters were calculated arithmetically and geometrically (in metric units, mean (M_G), mode (μm), median (D50 (μm), and sorting (σG)) and logarithmically (in phi units, mean (M_Z), mode (φ), median (D50 (φ), and sorting ($\sigma 1$)) using moment and Folk and Ward graphical methods (Blott and Pye 2001).

Lithological compositions and textures, as well as provenance studies of the sandstones, were determined by petrographic and modal analysis by counting 400 framework grains per thin section according to the Gazzi-Dickinson method (Ingersoll et al. 1984; Zuffa 1985, 1987) (see Table 3). Eolian sandstone classification was determined using the QFL ternary diagram proposed by Garzanti et al. (2018) in which eighteen categories of fields are recognized. The ternary diagram of Dickinson et al. (1983) was used to analyze provenance.

Paleowind velocities were calculated utilizing the formula proposed by Bagnold (1941):

$$V_{*_{(t)}} = A^{*}\sqrt{\frac{\rho_s - \rho_a}{\rho_a} * g * d} \quad (1)$$

where $V_{*(t)}$ represents the critical paleowind shear velocity. This parameter represents the minimum speed threshold needed for grains lying on the

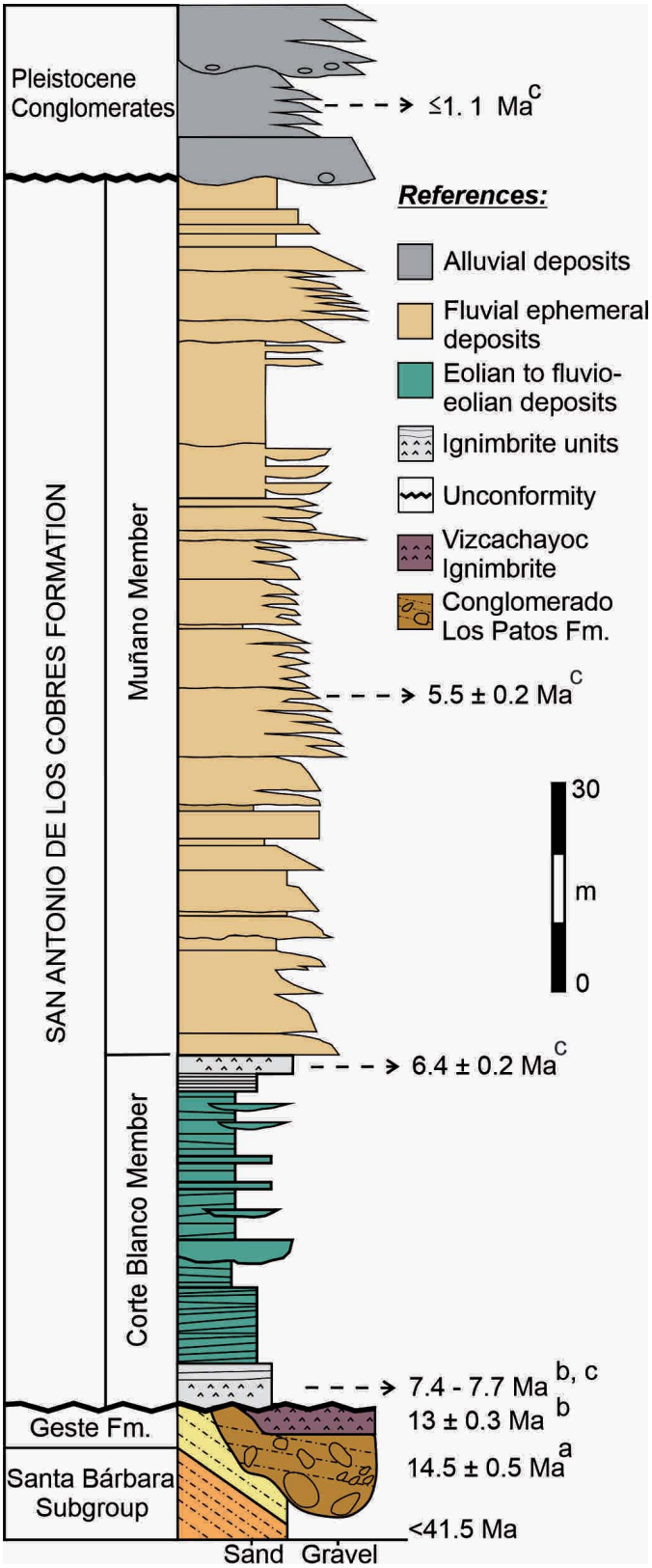

FIG. 3.—Synthesized stratigraphic column of the San Antonio de los Cobres Formation showing the main sedimentary characteristics and its stratigraphic relationships at the type area. Reported ages are from: a, del Papa and Petrinovic (2017); b, Petrinovic et al. (1999); c, Pingel et al. (2019).

substrate surface to start to move or travel, and it is closely linked to the textural characteristics of the sediment since it should vary as the square root of the grain diameter (Bagnold 1941). A is an experimental coefficient with a value of 0.1 for particles larger than 0.1 mm. The parameter ρ_s corresponds to the density of a grain of quartz, which is 2650 kg/m^3. This choice is based on the fact that the eolian sands of the Corte Blanco Member are abundant in quartz as well as K-feldspar and plagioclase (densities of 2500–2600 kg/m^3 and 2600–2700 kg/m^3, respectively). ρ_a is air density at a value of 0.87 kg/m^3 at an elevation of 3400–3500 m.a.s.l. (López Steinmetz and López Steinmetz 2018). The g parameter corresponds to acceleration due to gravity, and d is the particle diameter.

To calculate the paleowind speed threshold at a height z above the surface, the formula proposed by Bagnold (1941) (Eq. 2) and the one proposed by Pye and Tsoar (2009) (Eq. 3 and 3a) were used with the objective of comparing them and testing the reliability of our data. The formula proposed by Bagnold (1941) (Eq. 2) is

$$v_t = 5.75 * V_{*(t)} * \log\frac{z}{k} \quad (2)$$

where 5.75 is a factor of proportionality between wind velocity and height (Bagnold 1941); $V_{*(t)}$ comes from Equation 1, z is the height above the surface, and k is the height of a focus where all the velocity lines converge, at which point the wind velocity is zero and is equal to $d/30$, where d corresponds to grain diameter. On the other hand, the formula from Pye and Tsoar (2009) is

$$U\Big/u_{*_{(t)}} = \frac{1}{k} * \ln\frac{z}{z_0} \quad (3a)$$

where $u_{*(t)}$ is the critical wind shear velocity, which is equal to $V_{*(t)}$, and therefore Equation 3a can be written as follows:

$$U = \frac{V_{*_{(t)}}}{k} * \ln\frac{z}{z_0} \quad (3b)$$

where U is the wind velocity at a height $z = 2$m above the surface; $V_{*(t)}$ comes from Equation 1, k is known as the *von Kármán universal constant* for turbulent flow, whose value is taken as 0.40 (von Kármán 1935; Tennekes 1973), and z_0 is the *roughness length* of the surface, which is approximately $d/30$, and d is the particle diameter.

To carry out these calculations, the mean grain size of each sample was taken into account (see Table 2, Textural statistics). Thus we obtained the parameters corresponding to the mean critical paleowind shear velocity ($V_{*(t)\ mean}$) and the mean paleowind velocity at a height z above the surface according to Bagnold (1941) ($v_{(t)\ mean}$), and according to Pye and Tsoar (2009) (U_{mean}), for each sample. Based on the premise that larger-diameter grains will need a higher wind-speed threshold to start movement, the diameter values used correspond to the maximum grain diameter determined in each sample and, therefore, the maximum critical paleowind shear velocity necessary to start moving a grain with a diameter equal to the maximum grain size of each sample ($V_{*(t)\ max}$) can be calculated. Consequently, the maximum wind speed at a height of two meters above the surface can be calculated for each sample according to Bagnold (1941) ($v_{(t)\ max}$) and to Pye and Tsoar (2009) (U_{max}) (See Table 4).

RESULTS

Eolian Stratigraphy and Spatial Distribution in the SAC Basin

Eolian and fluvio-eolian successions have only been identified in the southern and central areas of the SAC basin (Figs. 2A, B). In the Northern Los Patos section (Location 3), the exposed thickness is 110 meters, but in the southern Corte Blanco section (Location 1), the total thickness is only 50 meters. In Location 4 the exposed thickness is only 10 meters while in Location 5 there is no record of eolian deposits (Figs. 2, 4). In Location 5

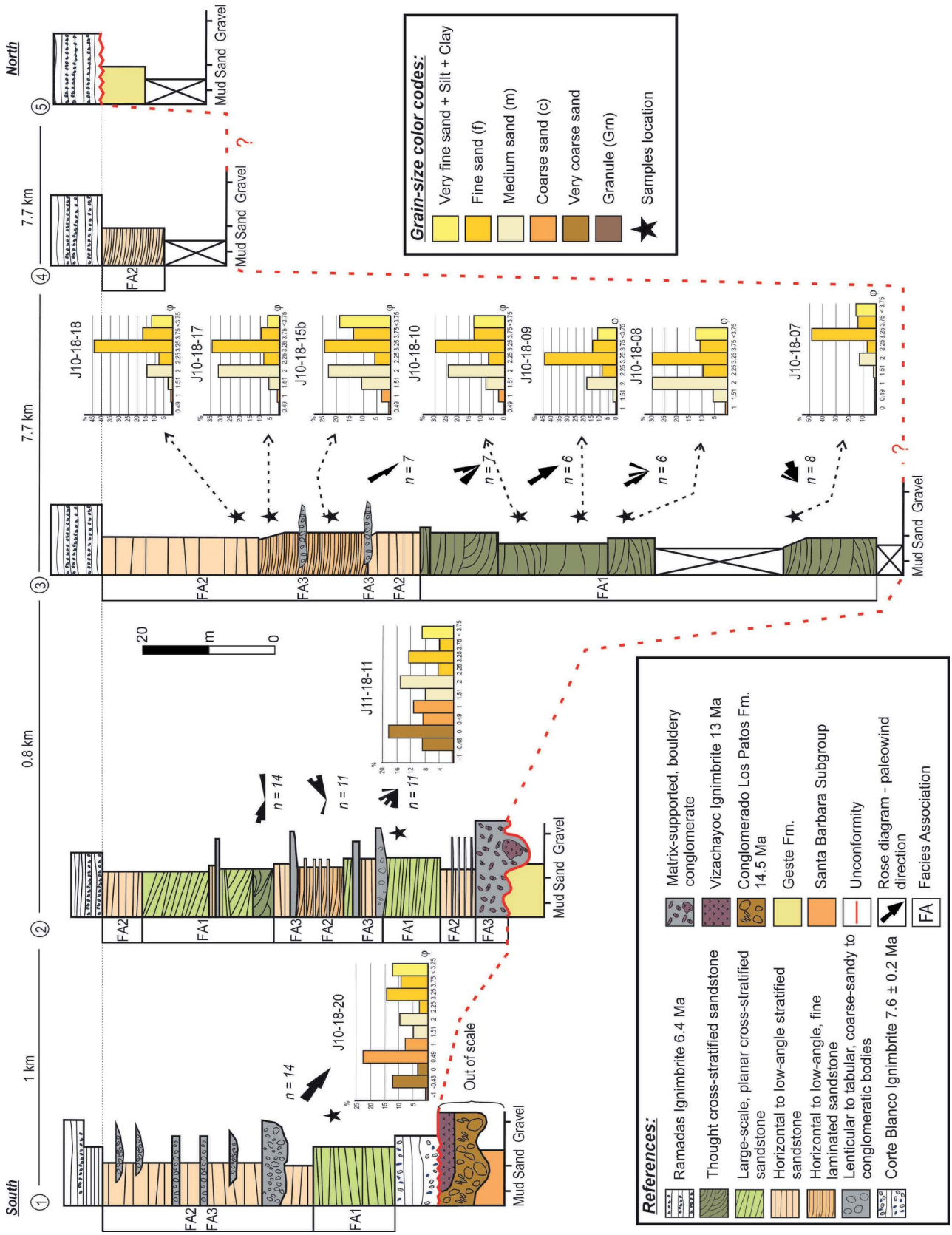

FIG. 4.—Stratigraphic logs of the Corte Blanco Member from Locations 1 to 5 (Fig. 1), highlighting the basal and upper contacts, the vertical and lateral facies changes, grain-size distribution of the eolian sandstones, and the calculated paleo-wind directions.

TABLE 1.—*Summary of eolian and fluvial sedimentary facies after Miall (1996) and Tripaldi (2012).*

Code	Description	Interpretation
Eolian facies		
St	Fine- to coarse-grained, trough cross-bedded sandstone with asymptotic basal terminations.	Migration of transverse dunes with sinuous crest lines.
Sp	Fine- to coarse-grained sand to granule sandstones, with large-scale tabular, planar cross-stratification.	Migration of transverse dunes with straight crest lines and lee faces dominated by grain-flow processes.
Sr	Very fine- to medium-grained sand with ripple lamination	Wind-ripple migration on eolian-sheet settings.
Sh	Fine to coarse, bimodal sandstone with fine, planar lamination or bedding. Ocasionally this facies shows inverse-grading layers.	Plane-bed lamination under high-wind velocities.
Fluvial Facies		
Sm	Medium-grained to gravelly sandstones with massive laminae/beds or normal-graded beds.	Flash-flood processes.
Gmm	Pebbly to bouldery, matrix-supported conglomerate, with no internal organization beds.	High-energy processes of debris flows or hyperconcentrated flows.
Gc/Gcg	Pebbly to cobbly, clast-supported conglomerate, with normal grading	Residual lag deposits of gravel bars in shallow channelized streams.

the Ramadas Ignimbrite lies on the Geste Formation, suggesting that eolian sedimentation did not reach this part of the basin. A similar stratigraphic relation is found toward the east of the basin. These thickness variations and distribution along the basin denotes a N–S wedge-shaped geometry in these deposits (Fig. 4).

The eolian unit lies on a prominent basal angular ($\sim 20°$) unconformity. In the Corte Blanco section, the SAC Formation rests on the middle Miocene Vizcachayoc Ignimbrite and on the middle Miocene Conglomerado Los Patos Formation; laterally ($\sim$ 1500 m towards the north), the strata below this contact change to the middle Eocene Geste Formation (Fig. 4). This basal angular to deep-erosional unconformity highlights the existence of active tectonism before to 7.8 Ma and pronounced paleotopography (Fig. 4). The top of the eolian unit is with the Ramadas Ignimbrite, which covers and seals the eolian and older deposits at ca. 6.4 Ma throughout the basin (Figs. 3, 4). After that eruptive event, there is no record that the eolian sedimentation was re-established.

Sedimentology and Facies Analysis

The eolian sandstone strata are extremely variable in grain size, from fine-grained sand to granules, and from poor to moderately well sorted (Fig. 4). Based on textural characteristics and sedimentary structures, we identified seven lithofacies (Table 1), assembled into three facies associations (FA):

Facies Association 1.—This facies association is composed of cross-stratified sandstones with large- to small-scale tabular, planar cross-bedding (Sp) (Fig. 5A–C), and of sandstones with trough cross-stratification (St) (Fig. 5C, D). The Sp facies is characterized by thick (2 to $>$ 10 m approx.) sets with tabular, planar cross-stratification, dipping $\sim$ 15–25°. Foresets are limited by nearly horizontal, first-order bounding surfaces; occasionally, some levels display second-order bounding surfaces (Fig. 5A–C). Internal lamina or bed thickness ranges from a few millimeters to $\sim$ 20 centimeters, typically inversely graded (Fig. 6A) or massive. The St facies is composed of small- to medium-scale sets and cosets of wedge or bowl shapes limited by concave-up second-order (and sometimes third-order) bounding surfaces (Fig. 5C, D). The grain size in the Sp facies ranges from fine sand to granules, with poorly to moderately well-sorted fabrics (Fig. 6B), whereas the St facies shows fine- to coarse-grained and moderately to well-sorted sandstones. Occasionally, there are low-relief lobate bodies (a few centimeters high and up to 60 cm wide) comprising coarser material, generally coarse-grained sand or granules with inverse grading (Fig. 6A, B).

TABLE 2.—*Textural sample statistics.*

Sample Name:		J10-18-07	J10-18-08	J10-18-09	J10-18-10	J10-18-15b	J10-18-17	J10-18-18	J10-18-20	J11-18-11
Mean (M_G):	μm	138.4	171	150.3	166.1	161.7	188	146.2	320.1	410.7
Sorting (σ_G):		1.73	1.823	1.723	1.915	2.004	1.727	1.733	3.048	2.873
Mean (M_1):	φ	2.853	2.548	2.734	2.59	2.628	2.412	2.774	1.643	1.284
Sorting (σ_1):		0.791	0.867	0.785	0.937	1.003	0.788	0.793	1.608	1.522
Mode 1 (μm):		67	300	157.5	300	67	300	157.5	855	1200
Mode 2 (μm):		157.5	67	67	67	300	157.5	67	67	300
Mode 3 (μm):		—	—	300	157.5	—	67	—	1700	67
Mode 1 (φ):		3.908	1.757	2.752	1.757	3.908	1.757	2.752	0.247	-0.243
Mode 2 (φ):		2.752	3.908	3.908	3.908	1.757	2.752	3.908	3.908	1.757
Mode 3 (φ):		—	—	1.757	2.752	—	3.908	—	-0.743	3.908
D_{50} (μm):		141.8	192.5	152.1	176.9	172.9	200.8	145.8	386.9	445.1
D_{50} (φ):		2.818	2.377	2.717	2.499	2.532	2.316	2.778	1.37	1.168
% V Fine Gravel:		0.00%	0.00%	0.00%	0.00%	0.00%	0.00%	0.00%	0.30%	0.40%
% V Coarse Sand:		0.10%	0.00%	0.00%	0.00%	0.00%	0.00%	0.00%	15.60%	27.10%
% Coarse Sand:		0.80%	0.70%	0.20%	2.90%	3.50%	1.40%	1.40%	30.50%	19.90%
% Medium Sand:		15.00%	35.80%	20.20%	32.60%	33.90%	38.10%	17.40%	14.60%	23.00%
% Fine Sand:		42.90%	32.40%	42.10%	30.10%	24.10%	35.10%	41.20%	13.60%	13.80%
% V Fine Sand:		38.30%	28.60%	35.20%	31.90%	34.90%	24.10%	37.80%	22.90%	14.10%
% Silt + Clay		3.00%	2.40%	2.20%	2.60%	3.70%	1.30%	2.30%	2.40%	1.70%

TABLE 3.—*Modal counting and lithological sandstone compotitions.*

		Monocrystaline Quartz					Lithics							
Sample Q/F/L %	Total (%)	Straight Extitniton	Undoluse Extitntion	Polycrystaline Quartz	K-Feldespar	Plagioclase	Volcanic	Sedimentary	Metamorphic	Opaque	Matrix	Biotite	Hornblende	Muscovite
J10-18-07	400	72	55	15	29	52	33	28	28	25	41	22	—	—
46/26/28	100%	18.00	13.75	3.75	7.25	13.00	8.25	7.00	7.00	6.25	10.25	5.50	—	—
J10-18-08	400	152	17	3	49	81	9	9	22	9	17	32	—	—
50/38/12	100%	38.00	4.25	0.75	12.25	20.25	2.25	2.25	5.50	2.25	4.25	8.00	—	—
J10-18-09	400	151	9	2	64	60	31	33	9	8	8	21	4	5
45/36/19	100%	37.75	2.25	0.50	16.00	15.00	7.75	8.25	2.25	2.00	2.00	5.25	1.00	1.25
J10-18-10	400	136	9	—	88	79	10	30	9	5	13	22	—	—
40/46/14	100%	34.00	2.25	—	22.00	19.75	2.50	7.50	2.25	1.25	3.25	5.50	—	—
J10-18-11	400	79	35	—	75	43	36	53	29	16	10	24	—	—
32/34/34	100%	19.75	8.75	—	18.75	10.75	9.00	13.25	7.25	4.00	2.50	6.00	—	—
J10-18-12	400	135	25	6	65	73	61	13	10	4	—	8	—	—
42/36/22	100%	33.75	6.25	1.50	16.25	18.25	15.25	3.25	2.50	1.00	—	2.00	—	—
J10-18-15A	400	100	14	10	87	81	11	5	29	6	11	46	—	—
37/50/13	100%	26.00	3.50	2.50	21.75	20.25	2.75	1.25	7.25	1.50	2.75	11.50	—	—
J10-18-17	274	49	11	—	80	59	5	10	15	6	17	22	—	—
26/61/13	100%	17.88	4.01	—	29.19	21.53	1.82	3.65	5.47	2.19	6.20	8.03	—	—
J10-18-18	400	127	26	1	60	76	20	10	46	11	12	11	—	—
42/37/21	100%	31.75	6.50	0.25	15.00	19.00	5.00	2.50	11.50	2.75	3.00	2.75	—	—
J10-18-20	400	192	20	10	62	24	23	5	36	—	21	7	—	—
60/23/17	100%	48.00	5.00	2.50	15.50	6.00	5.75	1.25	9.00	—	5.25	1.75	—	—
J03-18-09	400	175	9	7	67	69	20	10	22	4	10	5	2	—
50/36/14	100%	43.75	2.25	1.75	16.75	17.25	5	2.5	5.50	1.00	2.50	1.25	0.50	—

Interpretation.—This facies association represents the migration of large- to medium-scale, cross-stratified transverse sand dunes with straight and sinuous crestlines and small, superimposed bedforms. Lee faces are dominated by avalanche (grain-flow) processes (Hunter 1977; McKee 1979; Rubin and Hunter 1983). Dispersive pressure generated by particle collisions during avalanches expelled coarser grains to the upper surface of the avalanche, resulting in slightly coarsening-upward deposits. These deposits recline close to the angle of repose on the lee sides of dunes and are thinner towards the base of the dune (Bristow and Mountney 2013). Fluctuations in the wind regime are documented by the presence of second-order bounding surfaces (migration of smaller bedforms across the lee face of the main bedforms) and third-order bounding surfaces (which represent reactivation surfaces) within cosets, resulting in complex sand bodies (Rubin and Hunter 1983; Kocurek 1991; Brookfield 1997).

Facies Association 2.—This facies association is composed of sandstones with planar to low-angle stratification (Sh) and by flat to slightly inclined, thinly laminated ripple sandstone strata with inverse grading (Sr) (Figs. 5C, 6C, D). Sandstone layers consist of fine- to coarse-grained, moderately sorted sand, arranged in parallel, thin bimodal laminae.

TABLE 4.—*Paleowind velocities.*

Sample	D_{mean} (mm)	$V_{*t\ mean}$ * (cm/s)	$v_{t\ mean}$ * (km/h)	U_{mean} ** (km/h)	D_{max} (mm)	$V_{*t\ max}$ * (cm/s)	$v_{t\ max}$ * (km/h)	U_{max} ** (km/h)
J10-18-07	0.14	21.17	24.78	24.71	1	54.65	54.05	54.11
J10-18-08	0.17	22.53	25.68	25.9	0.5	38.65	40.63	40.68
J10-18-09	0.15	21.17	24.55	23.58	0.5	38.65	40.63	40.68
J10-18-10	0.16	21.86	25.22	25.25	0.71	46.05	46.97	47.02
J10-18-15b	0.16	21.86	25.22	25.25	0.71	46.05	46.97	47.02
J10-18-17	0.19	23.82	27.11	27.14	0.71	46.05	46.97	47.02
J10-18-18	0.14	21.17	24.78	24.71	0.71	46.05	46.97	47.02
J10-18-20	0.32	30.92	33.75	33.79	2	77.29	71.62	71.71
J11-18-11	0.41	35	37.42	37.44	2	77.29	71.62	71.71

After Bagnold (1941)* After Pye and Tsoar (2009)**

Interpretation.—This facies association is interpreted as having been deposited in an eolian sandsheet setting dominated by wind-ripple migration (Hunter 1977; Kocurek and Nielson 1986; Kocurek 1991).

Facies Association 3.—This facies association is characterized by tabular, medium- to coarse-grained, massive sandstones (Sm) (Fig. 6E–G) associated with lenticular beds of pebbly to bouldery, matrix-supported conglomerates (Gmm) (Fig. 6E, G, H) and by poorly sorted, pebbly to cobbly, clast-supported conglomerate with normal grading (Gc/Gcg) (Fig. 6F). The Gmm facies is composed of angular to subangular clasts of up to 2 meters, floating with no preferential organization in a fine-grained greenish matrix (Fig. 6E, G, H). These conglomerate beds are composed of grayish to blackish fiamme-rich ignimbrite, low-grade metamorphic, quartz-rich sandstones, and bluish slate clasts (Fig. 6F).

Interpretation.—This facies association represents deposition from gravitational debris flows (Gmm) and hyperconcentrated flows (Sm), as well from normal dilute flows (Gcg) in interdune areas. The presence of debris and hyperconcentrated flows suggests ephemeral currents probably associated with sporadic rains that flooded the interdune areas (Bristow and Mountney 2013). Moreover, the occurrence of well-organized deposits points to shallow channelized streams.

Grain-Size Characterization

Samples from the Northern Los Patos site (Site 3 in Fig. 2B) are fine to very fine sand with $> 50\%$ in weight corresponding to grain sizes of 74 to < 250 μm (3.75 and < 2 φ) (Fig. 4, Table 2). All samples analyzed show bimodal distribution except for samples J10-18-09/10/17, which have trimodal composition, with modes at 67, 157.5, and/or 300 μm, or 3.908, 2.752, and/or 1.757 φ, respectively. Sandstones are moderately sorted, with values ranging between 1.723 and 1.915 σG or 0.785 and 0.937 $\sigma 1$, except

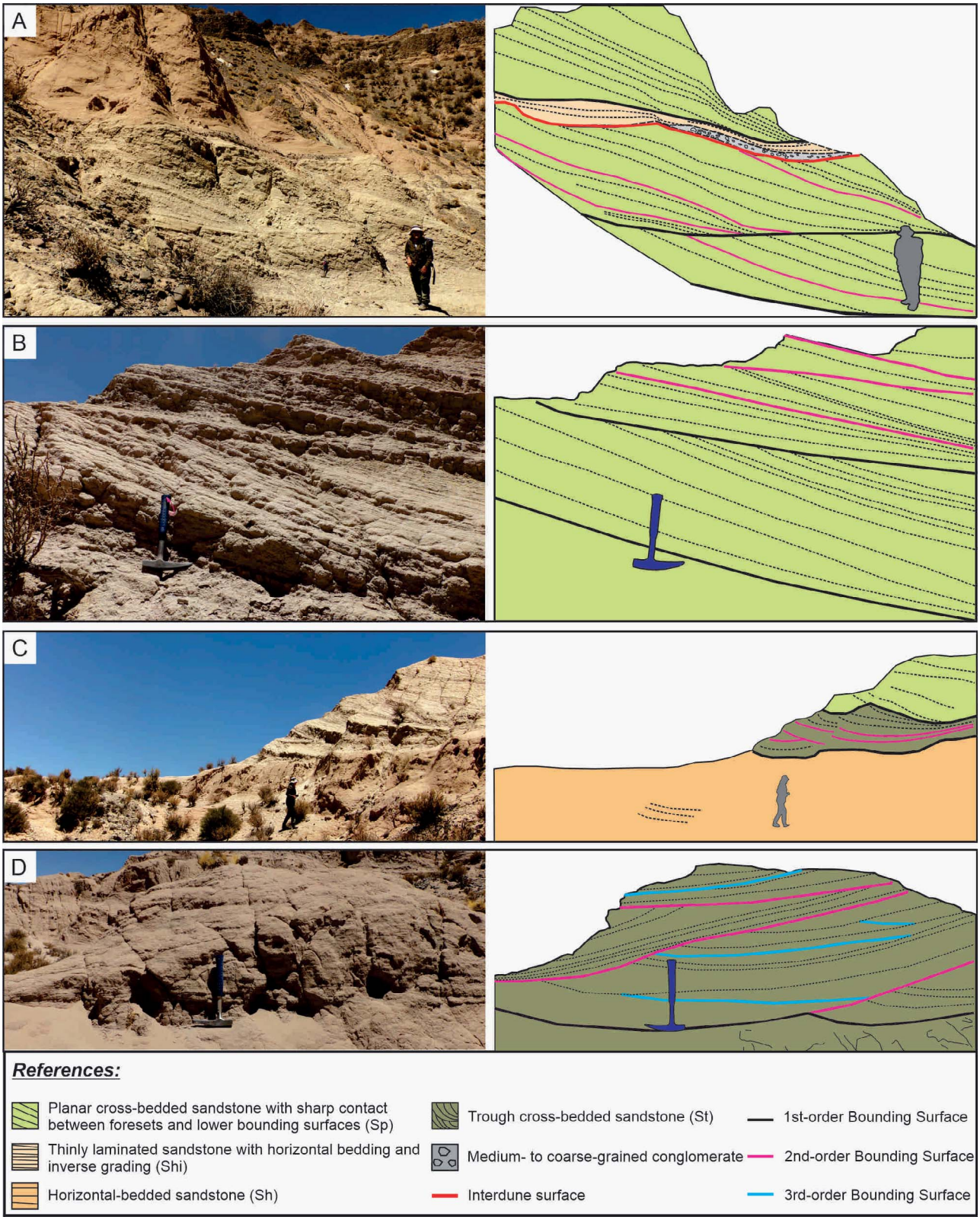

FIG. 5.—Sedimentary facies and main bounding surfaces of the Corte Blanco Member. See text for further explanation. **A)** Cosets of Sp facies containing 1st- and 2nd-order bounding surfaces. These cosets are capped by an interdune surface with a conglomerate lag deposit of Gc facies and Sm facies. The top of the succession is composed of a large-scale set of sandstone of Sp facies. **B)** Cosets of Sp facies limited by 1st-order bounding surfaces and with internal 2nd-order bounding surfaces formed by superimposition of bedforms. **C)** Thick set of Sh facies overlain by a small coset of Sp and St facies, representing small superimposed bedforms. **D)** Coset of St facies with sets separated by 2nd-order bounding surfaces, with internal 3rd-order bounding surfaces. The lower surface corresponds to a composite 1st-order bounding surface formed by 2nd-order bounding surfaces.

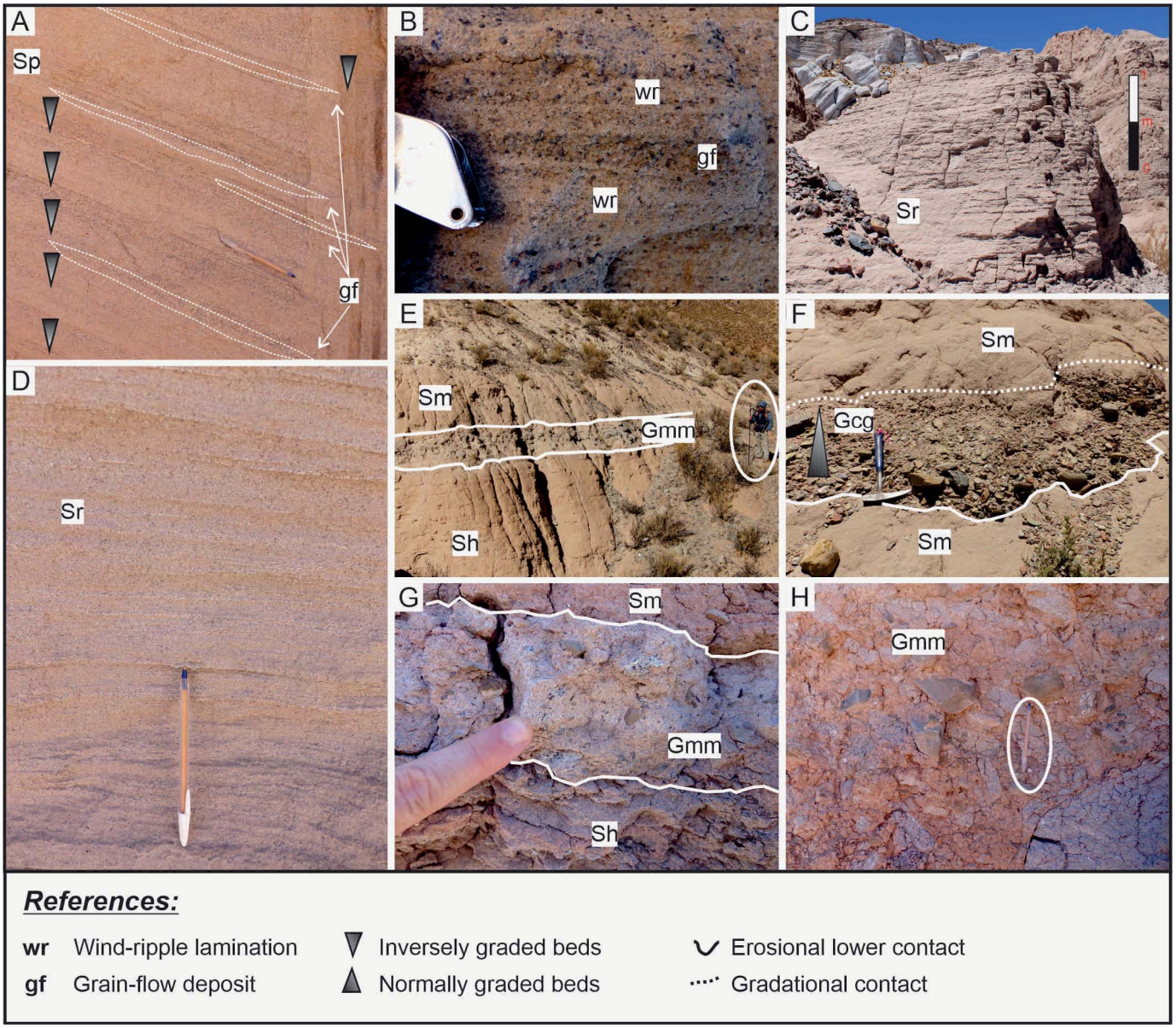

FIG. 6.—Sedimentary facies of the Corte Blanco Member. **A)** Thick strata of Sp facies composed of medium- to coarse-grained sand with inverse grading and small, lobate bodies that represent deposits by grain-flow (gf) process. **B)** Wind-ripple (wr) and grain-flow wedge (gf) on a coarse-grained to granule sandstone. Hand lens as scale. **C**, **D)** Sets of sandstone with fine, planar wind-ripple lamination (Sr). **E)** Tabular, matrix-supported, pebbly to cobbly conglomerate interbedded with thick sets of sandstones with planar stratification (Sh) and massive sandstones (Sm). **F)** Lenticular deposit of clast-supported, pebbly to bouldery conglomerate with inverse grading (Gcg), interbedded with massive sandstone (Sm). **G)** Thin, tabular, matrix-supported conglomerate (Gmm) interbedded with planar-stratified sandstones (Sh) and massive sandstone (Sm). **H)** Cobbly to bouldery, matrix-supported conglomerate. Some clast are > 2 m in diameter.

for one sample (J10-18-15b) with a value of 2.004 σG or 1.043 $\sigma 1$ classified as poorly sorted.

On the other hand, sample J11-18-11, from the Southern Los Patos site (Site 2 in Fig. 2B), is very poorly sorted (2.837 σG–1.522 $\sigma 1$) and is polymodal with three main modes at 1200, 300, and 67 μm or –0.243, 1.757, and 3,908 φ (Fig. 4). This sample comprises medium-grained sand (23%), coarse sand (19.9%), very coarse sand (27.1%), and granules (0.4%) (see Table 2).

Finally, sample J10-18-20, from the Corte Blanco site (Site 1 in Fig. 1C) is polymodal, with 3 main modes at 855, 67, and 1700 μm or 0.247, 3.908, and –0.743 φ. The main classes are coarse sand (30.5%) and very fine sand (22.9%).

Interestingly, the coarsest sand grains (coarse sand to granules) are found in the same lithofacies (Sp) at both Sites 1 and 2 (Fig. 4), whereas at Site 3, such coarse sand grains are not found. At this site, the main facies correspond to St and Sh and the main grain sizes vary from very fine sand to medium sand.

Sandstone Composition and Provenance

The eolian sandstones of the Corte Blanco Member are characterized by angular to subangular grains and open-framework fabrics (Fig. 7A, B). The cement is commonly siliceous, but ferruginous and clayey coatings can also occur on grains (Fig. 7C). Sandstones are composed mainly of quartz

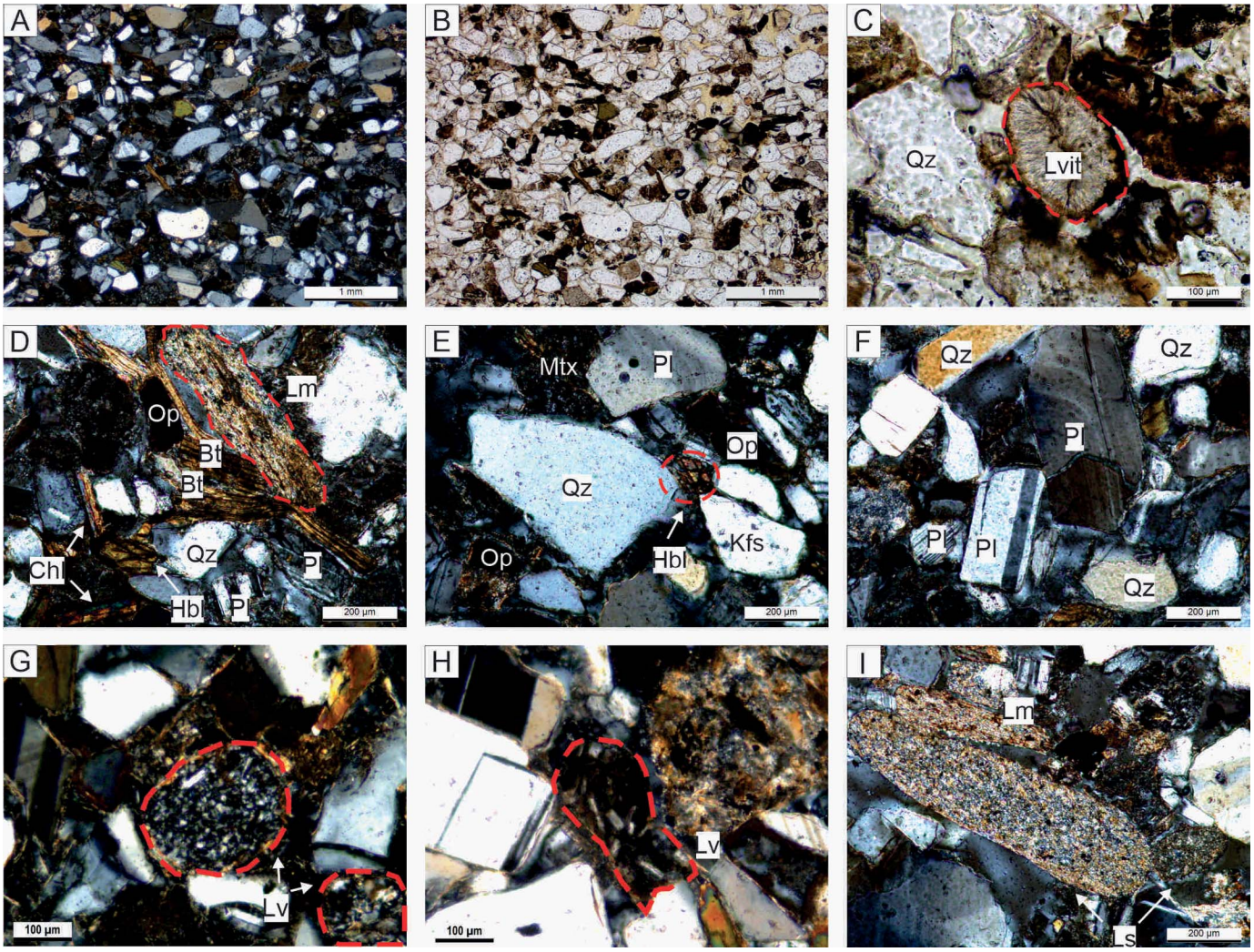

FIG. 7.—Microphotographs showing sandstone compositional types. **A**, **B)** General view of angular to subangular grains and open-framework fabrics. **C)** Vitric volcanic lithic surrounded by reddish ferruginous and clayey coatings. **D**, **E)** Subangular grains of the main and accessory constituent minerals. Biotite grains are deformed due to compaction effects. **F)** In the central part of the image there is a zoned tabular plagioclase crystal, and to the left of it two plagioclase grains with polysynthetic twinning. **G)** Paleovolcanic lithic fragments. **H)** Neovolcanic lithic fragments with micro-porphyritic texture and tabular phenocrysts of plagioclase and aphanitic darkish matrix. **I)** Metamorphic lithic fragments at the top of the image, with flattened shape and inner lamination. At the bottom of the image there are two sedimentary lithic fragments.

(monocrystalline and polycrystalline), K-feldspars, and plagioclase as well as lesser amounts of lithics of volcanic, plutonic, metamorphic, and sedimentary origin. Accessory minerals include biotite, chlorite, muscovite, and hornblende (Fig. 7D, E, Table 3). Quartz frequently occurs as monocrystalline grains (Fig. 7E), showing both flash and undulose extinctions, whereas polycrystalline quartz is not very common. K-feldspar minerals include orthoclase and microcline (Fig. 7E). Orthoclase appears either as untwinned or twinned crystals, whereas microcline exhibits typical tartan twinning. Plagioclase usually show polysynthetic twinning and zoning (Fig. 7D, F). Among the volcanic lithics, paleovolcanic lithics show granular textures made up of recrystallized quartz, K-feldspar, and biotite (Fig. 7G), and neovolcanic fragments show micro-porphyritic textures with phenocrysts of plagioclase or K-feldspar and a dark to grayish aphanitic matrix (Fig. 7H). Volcanic vitric shards are also present (Fig. 7C). Metamorphic lithics are usually fragments of slate or schist and have a characteristic flattened shape and laminated internal structure (Fig. 7D, I). Sedimentary lithics consist of quartz-rich sandstone fragments (Fig. 7I).

Sandstones are classified as litho-feldespatho-quartzose (lFQ) and litho-quartzo-feldespathic (lQF), according to Garzanti et al. (2018) (Fig. 8A). Furthermore, sandstone compositions indicate that they were derived from the Dissected Magmatic Arc and Recycle Orogen compositional fields (Fig. 8B) (Dickinson et al. 1983). Mineral associations suggest that the material for the eolian sand derived from Paleozoic and Miocene magmatic rocks as well as from Neo-Proterozoic to Paleozoic low-grade metamorphic and sedimentary rocks.

Paleowind Regime

Predominant paleowinds were north-northwesterly (310–330°), with minor easterly winds (70–90°), which show no meaningful changes in winds over time and space (see Figure 4 for rose diagrams for each set of measurements).

As previously noted, two approaches were taken into account to calculate the Miocene paleowind velocities in this part of the Puna Plateau. After performing the calculations with both methods—Bagnold (1941) and Pye and Tsoar (2009)—it is evident that the two formulas provide similar

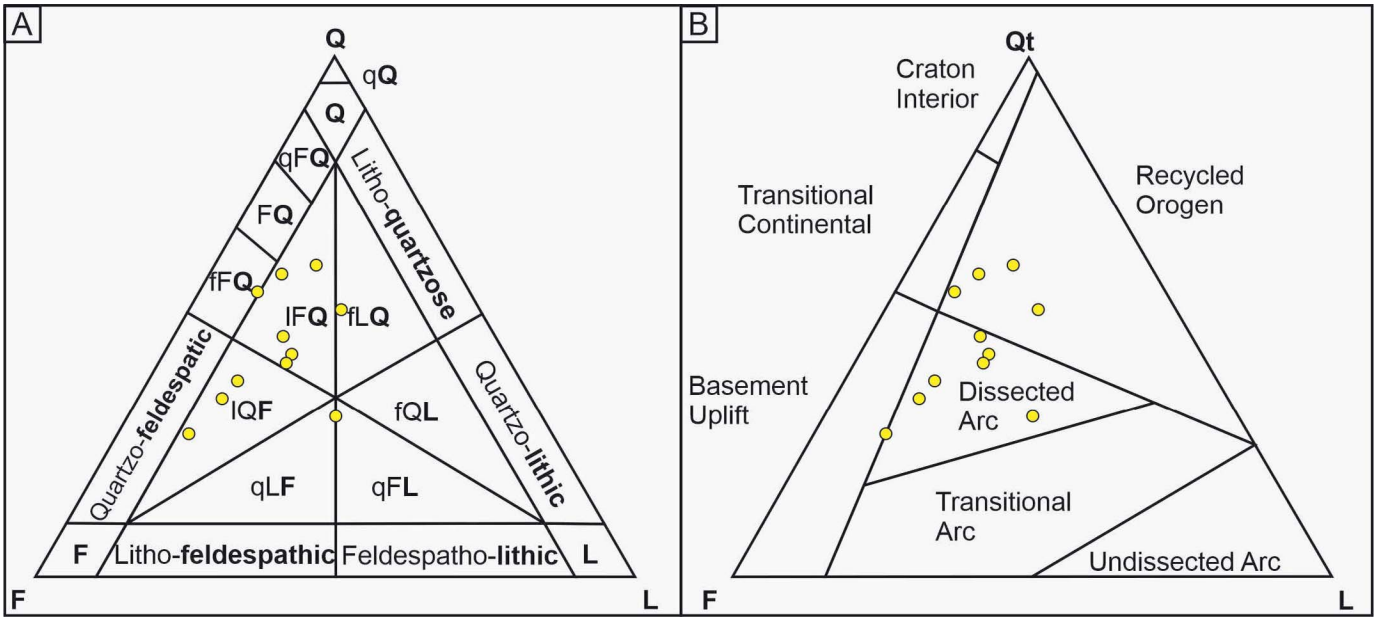

FIG. 8.—**A)** Sandstone classification proposed by Garzanti et al. (2018). Q, quartzose (qQ, pure quartzose); F, feldspathic; L, lithic; FQ, feldspatho-quartzose (fFQ, feldspar-rich; qFQ, quartz-rich); QF, quartzo-feldspathic; LF, litho-feldspathic; FL, feldspatho-lithic; QL, quartzolithic; LQ, litho-quartzose; lFQ, litho-feldspatho-quartzose; lQF, litho-quartzo-feldspathic; qLF, quartzo-litho-feldspathic; qFL, quartzo-feldspatho-lithic; fQL, feldspatho-quartzo-lithic; fLQ, feldspatho-litho-quartzose. **B)** Tectonic discrimination diagram after Dickinson (1983).

results for the same paleowind critical shear speed for a certain particle diameter (Table 4). Taking into account the maximum grain size reported in the eolian sandstones of the Corte Blanco Member (2 mm), the minimum critical paleowind shear velocity necessary to start movement is $V_{*(t)} = 77.29$ cm/s (Table 4). Assuming ideal conditions, that is, flat, dry surfaces, unconsolidated and noncohesive sediments, and/or the absence of vegetation, the corresponding maximum wind speed at a height of 2 meters above the surface is $v_{*(t)max} = 71.62$ km/h (Bagnold 1941) or $U_{max} = 71.71$ km/h (Pye and Tsoar 2009) (Table 4). This paleowind speed is very close to the maximum current wind speed of 80 km/h reported for this area (López Steinmetz and López Steinmetz 2018).

PALEOENVIRONMENTAL INTERPRETATION

The Corte Blanco Member represents the only eolian record in the San Antonio de los Cobres basin. The prominent basal angular unconformity (Figs. 4, 9) highlights tectonic activity preceding its deposition, and effective weathering and erosional processes that modeled the landscape. The thickness of this member varies along strike (north to south), with the thinnest strata to the north (Site 5 in Figs. 2, 4) and the thickest deposits in the south-central part of the basin (Sites 1, 2, and 3 in Figs. 2, 4). This highly lenticular geometry and basal contact relationships suggest that the eolian sandstones were deposited on a paleo-relief (Figs. 4, 9).

Based on the lateral assemblages of the facies associations, we interpret an eolian environment dominated mainly by transverse dunes with sinuous crestlines and minor dunes with straight crestlines (FA1) associated with eolian sandsheet (FA2) and wet interdune areas (FA3) near the margin of the field (Fig. 9). This interpretation is consistent with fluvio-eolian interaction sedimentary models described by Langford and Chan (1989) and Tripaldi and Limarino (2005). Moreover, and taking into account vertical facies changes, we interpret two evolutionary stages:

Stage 1.—This stage was dominated by the migration of transverse dunes with sinuous to straight crest lines (FA 1) associated with lateral sandsheets (FA 2) and debris-flow processes (FA 3) to the margins of the field (Fig. 9).

Stage 2.—This stage was dominated by an eolian sandsheet setting (FA 2) laterally associated with an ephemeral fluvial system (FA 3). The eolian sedimentation was sharply terminated by the Ramadas Ignimbrite volcanic event that covered the basin at 6.4 Ma.

The integration of petrographic and paleowind data implies that source areas are located toward the north-northwest of the SAC basin. In this direction, there are exposures of metamorphic and metasedimentary rocks of the Neo-Proterozoic Puncoviscana Formation, and sedimentary rocks of the Late Cambrian Meson and Early to Middle Ordovician Santa Victoria groups as well as Ordovician granitoids of the Oire Eruptive Complex, which extends in a N–S trending belt (Fig. 10B; Turner 1964; Seggiaro et al. 2015). These units could have provided the quartz-rich sand and the sedimentary and metamorphic lithics. However, among the volcanic lithics we differentiated two sources, one from the Ordovician volcanic arc and a second one from the Miocene volcanic arc (Fig. 7C, G, H). Ordovician volcanic grains are characterized by intense silicification due to recrystallization of the volcanic glass (Fig. 7G), whereas Miocene grains frequently have a lathwork texture (Fig. 7H) with clean, tabular phenocrystals in a darkish glass groundmass.

In contrast to the eolian sandstones, the composition of the fluvial conglomerate indicates a mainly volcanic origin (Fig. 6E, H). Based on the component clast characteristics, such as a high degree of weld and the abundant juvenile fragments, the most probable volcanic source is the Vizcachayoc Ignimbrite.

Paleocurrent analysis indicates northwesterly winds in accordance with the lithotypes and mineralogical composition of sandstones, suggesting a provenance from the Miocene western volcanic arc and from Paleozoic metasedimentary and granitic units. The consistent angular to subangular textures common in sand grains suggest proximal source areas and minimal recycling of older grains. Toward the north and northwest of the study area, the granitoids of the Oire Eruptive Complex and volcanic rocks from Miocene ignimbrites in the Susques area crop out (Seggiaro et al.

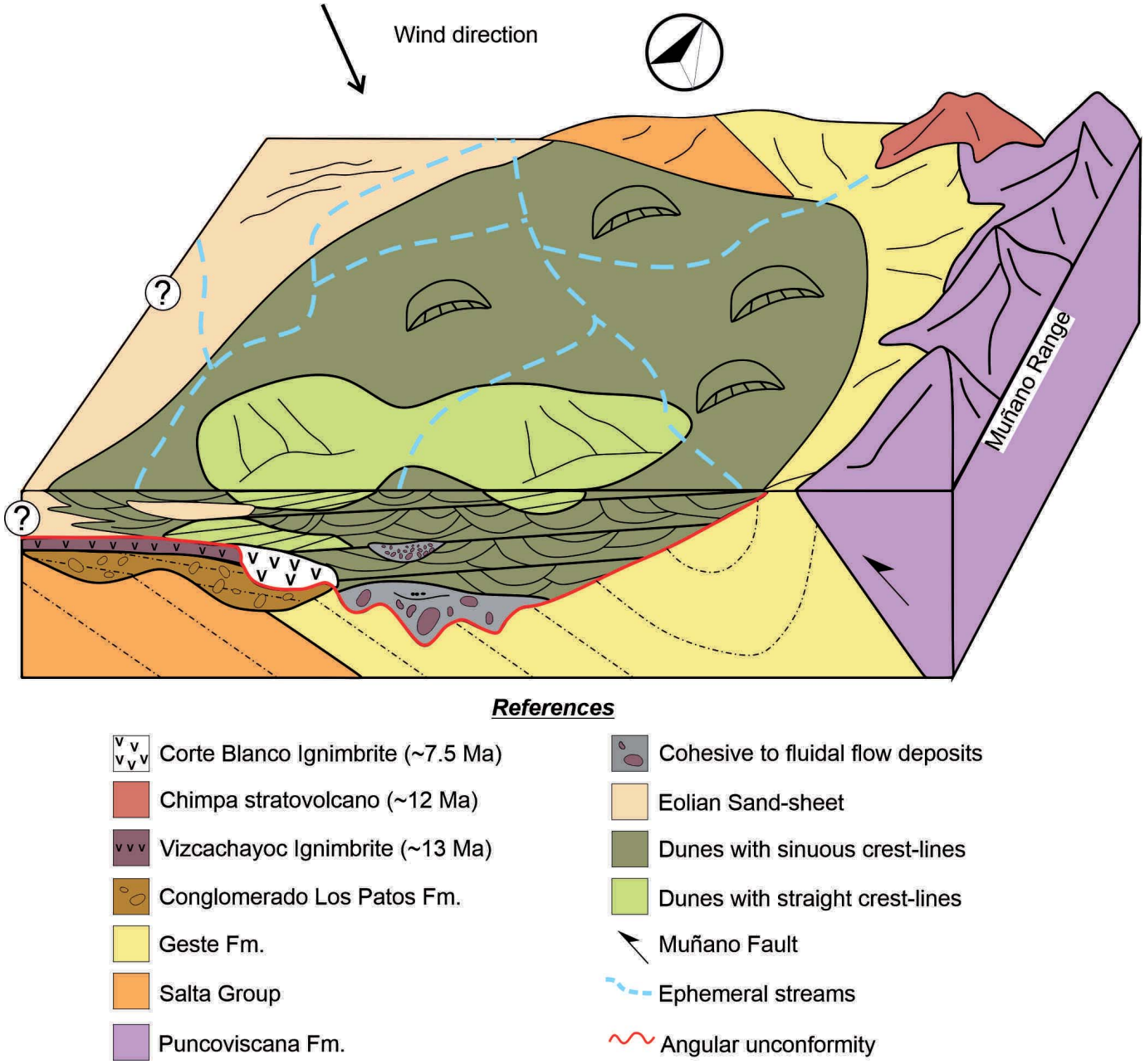

FIG. 9.—Block diagram of the paleoenvironmental interpretation for end of the Stage 1 of the late Miocene eolian field in the SAC basin showing the main units and the basal contact relationships. Toward the north, east, and west of the basin there is no evidence of eolian sedimentation while the thickest deposits occur towards the central to southern areas (Locations 1, 2, and 3 in Fig. 4), delineating a N–S-trending, wedge-shaped paleogeometry for the basin.

2015), representing the most plausible source for this eolian field (Fig. 10B).

DISCUSSION

The eolian record in northwestern Argentina is characterized by late Oligocene to late Miocene sandy deposits and by broadspread evidence of late Miocene to Present deflation processes. Thick, late Oligocene to early Miocene sandy eolian deposits showing consistent westerly paleowinds extend along the Puna Plateau, the Eastern Cordillera, and the Santa Bárbara System to the east (Fig. 10A, C_2). In the Salina del Fraile and Sierra de Calalaste regions on the southern Puna Plateau (Fig. 10A), for instance, the Chacras Formation contains an ~ 150-m-thick eolian unit of ~ 22 Ma showing paleoflow directions from the west (Kraemer et al. 1999; Carrapa et al. 2005). Likewise, ~ 120-m-thick eolian deposits in the Lower Vizcachera Formation from the Arizaro basin (Fig. 10A) yield ages ranging between ca. 21–18 Ma with easterly and westerly paleowinds (DeCelles et al. 2015). Moreover, in the Eastern Cordillera, > 300-m-thick eolian deposits with ages from ca. 28 to 17 Ma and west-northwesterly paleowinds have been reported in the Angastaco Formation in the Calchaquí Region (Fig. 10A; DeCelles et al. 2011; Carrapa et al. 2012; del Papa et al. 2013a, 2013b; Payrola et al. 2020). Similarly, the ~ 15 Ma Río Seco Formation in the Lerma Valley from Eastern Cordillera (Fig.

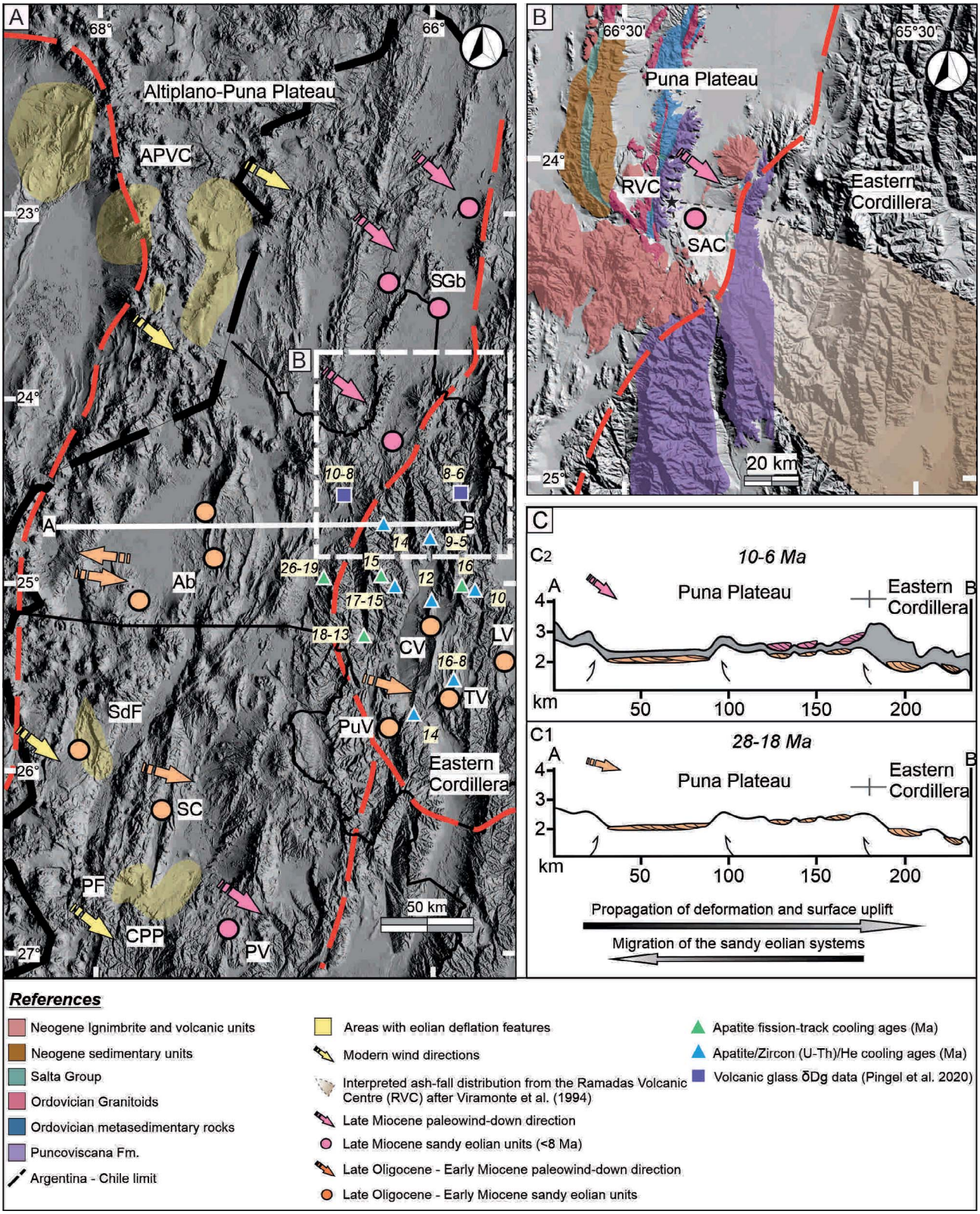

FIG. 10.—**A)** Digital elevation model (DEM) from NW Argentina showing the distribution of late Oligocene–early Miocene and late Miocene eolian units along the Puna Plateau and Eastern Cordillera, and the reported paleocurrent directions. APVC, Altiplano–Puna Volcanic Centre; SGb, Salinas Grandes basin; Ab, Arizaro basin; SdF, Salina del Fraile; SC, Sierra de Calalaste; PF, Purulla Field; CPP, Campo de Piedra Pómez; PV, Pasto Ventura; CV, Calchaquí Valley; LV, Lerma Valley; TV, Tonco Valley; PuV, Pucará Valley. AFT, AHe and ZHe thermocronological data were taken from Deeken et al. 2006; Carrapa et al. 2011; Pearson et al. 2012, 2013; Payrola et al. 2020, 2021. **B)** Digital elevation model (DEM) from the northern Puna Plateau showing the main lithological units towards the northwest of the SAC basin that could have been the source areas for the sandy eolian field developed on the SAC basin. After Blasco et al. (1996) and Seggiaro et al. (2015). **C)** Interpreted elevation profiles (after Hartley 2003; Pingel et al. 2020), and evolution and distribution of eolian systems in the Puna and Eastern Cordillera regions for the 1) late Oligocene–early Miocene (28–18 Ma) and 2) late Miocene (10–6 Ma) respectively.

10A) exhibit thick eolian strata (Starck and Vergani 1996; Reynolds et al. 2000).

On the other hand, late Miocene eolian units (~ 8–6 Ma) are thinner and restricted only to the eastern border of the Puna Plateau (Fig. 10A, C_1). For example, an ~120-m-thick eolian deposit of 7.7–7.8 Ma has been described in the Pasto Ventura region, southern Puna Plateau (Fig. 10A), showing a northwesterly paleowind direction (Schoenbohm and Carrapa 2015; Zhou et al. 2016). Interestingly, López-Steinmetz and López-Steinmetz (2018) described several eolian units of inferred late Miocene age north of the Salinas Grandes basin, on the northern Puna Plateau (Fig. 10A), revealing northwesterly paleowinds. In accordance with this data, our own paleowind data (Figs. 4, 10B) show that, for the ca. 7.8–6.5 Ma time period, the predominant winds were blowing from the north-northwest. Supporting the inference of late Miocene north-northwesterly winds, Viramonte et al. (1994) mapped the distribution of the ash fall from the Ramadas Volcanic Centre (RVC) in a southeast trend from its source (Fig. 10B).

In contrast to the late Miocene eolian sand sedimentation documented on the eastern Puna Plateau, eolian deflation processes have been reported on the western and southern Puna Plateau (Fig. 10A). McMillan and Schoenbohm (2020), for instance, reported large-scale wind-erosion processes that excavated the Salinas del Fraile depression from the middle–late Miocene to the present (Fig. 10A). Some studies have shown that strong, unidirectional winds from the north-northwest have been eroding the Altiplano–Puna Volcanic Complex (APVC) along northern Chile (Fig. 10A). In this area, evidence of eolian deflation processes modeled yardangs and elongated ridges over ignimbrite units of Pliocene–Pleistocene age (~ 5.3–1.35 Ma; Greene 1995; Bailey et al. 2007). Likewise, de Silva et al. (2010) found evidence of wind erosion over ignimbrite units of ca. 70–13 kyr in the Campo de Piedra Pómez (CPP in Fig. 10A) on the southern Puna Plateau. These authors highlight the consistent alignment between the yardangs and the modern wind direction (NW–SE). Furthermore, McMillan and Schoenbhom (2020) inferred a present-day northwestly predominant wind flow in the Salina del Fraile area, based on the alignment of geomorphological features such as yardangs and megaripples.

Present-day mid- to upper-level tropospheric circulation and precipitation patterns in the Altiplano–Puna Plateau region are regulated by the Bolivian High anticyclone over the Altiplano Plateau (Gutman and Schwerdtfeger 1965; Virji 1981; Lenters and Cook 1997). This anticyclone is characterized by seasonal behavior. During the austral summer (December to February), the Bolivian High becomes firmly established and displaced southward, generating strong northwesterly winds over the Puna Plateau and allowing moisture from the Amazon basin to reach this region. During the austral winter (June to August), this anticyclone is weakened and the prevailing strong, westerly winds prevent penetration of the moisture that easterly winds carry from the interior of the continent, generating cooler and drier conditions along the Puna–Altiplano Plateau (Lenters and Cook 1999; Vuille 1999; Fiorella et al. 2015). Presently, the Puna–Altiplano Plateau is a dust-producing region that feeds sediment to eastern areas as far as the Antarctic ice sheets and Atlantic Ocean (e.g., Gaiero 2007; Gaiero et al. 2013; Milana and Kröhling 2017). The dust movement is driven by the upper-troposphere westerly winds with speeds ranging between 19 and 80 km/h (Buitrago et al. 1999) and spiking at ~ 130 km/h (e.g., Gaiero et al. 2013). Interestingly, our data suggest that late Miocene paleowind velocities in the SAC basin were ~ 24–38 km/h, with maximum speeds of ~ 55–75 km/h, which coincide with the velocities reported by López Steinmetz and López Steinmetz (2018) for areas north of the study area (Fig. 10A).

Current atmospheric circulation over South America shows that the Andes mountain range acts as a large meridional orographic barrier to easterly moisture-bearing winds from the Atlantic Ocean and the Amazon basin (Strecker et al. 2007; Bookhagen and Strecker 2008; Mulch et al. 2010; Pingel et al. 2016; Rohrmann et al. 2016; among others). Due to this blockage, easterly winds are redirected along the orogen towards the south, forming the South American Low Level Jet (SALLJ) (Vera et al. 2006; Strecker et al. 2007; Rohrmann et al. 2016). Factors favoring the aridity on the Puna–Altiplano Plateau include the rain-shadow effect, major cooling related to changes in global oceanic circulation at ca. 15–10 Ma, and the reduction of moisture carried by the westerlies (Houston and Hartley 2003; Bookhagen and Strecker 2008).

The Altiplano–Puna Plateau has experienced uplift and eastward propagation of deformation since the Eocene–Oligocene (Kraemer et al. 1999; Coutand et al. 2001; Carrapa et al. 2005; Coutand et al. 2006; DeCelles et al. 2007; among others). The middle to late Miocene (~ 15–6 Ma) was a period of particularly intense tectonic activity and surface uplift in the eastern Puna Plateau and the Eastern Cordillera, supported by structural and thermo-chronological data (Fig. 10A; e.g., Allmendinger and Gubbels 1996; Haschke et al. 2005; Deeken et al. 2006; Carrapa et al. 2011, 2012; Pearson et al. 2012, 2013; Payrola et al. 2020, 2021). The establishment of the SALLJ at ca. 10–8 Ma (Mulch et al. 2010; Pingel et al. 2016; Rohrmann et al. 2016), and the rain-shadow effect at ca. 15–10 Ma (Hartley 2003; Houston and Hartley 2003), suggest that the eastern border of the Puna Plateau was already a high enough orographic barrier to cause a disturbance in lower-level paleo-tropospheric circulation. Supporting this, negative hydrogen-isotope shifts from volcanic glass (δDg) in rocks from the Pastos Grandes basin (Puna Plateau) and from the El Toro basin (Eastern Cordillera) reveal kilometer-scale surface uplift at 10–8 Ma for the Puna Plateau and at 8–6 Ma for the Eastern Cordillera, respectively (Fig. 10A, C; Pingel et al. 2020)

Our survey of late Miocene (8–6 Ma) sandy eolian deposits document that they were formed by consistent westerly to northwesterly winds (Fig. 10A). The distribution of these units as thin belts attached to the western flanks (windward side) of the present high mountains limiting the Puna Plateau–Eastern Cordillera border suggests a topographic control (Figs. 9, 10A, C).

The north-northwesterly paleoflow direction recorded by the late Miocene sandy eolian units around the Puna Plateau is in line with the present-day dominant winds (Gaiero et al. 2013; Milana and Kröling 2017; López Steinmetz and López Steinmetz 2018; McMillan and Schoenbohm 2020). Therefore, we suggest that the middle- to upper-troposphere circulation patterns have remained nearly constant for at least the last 8 Myr. In contrast to the sandy eolian accumulation along the eastern margin of the Puna Plateau, the western region was affected by deflation processes, evidenced by deflation surfaces, yardangs, and wind-derived northwest–southeast-trending linear ridges (Bailey et al. 2007; de Silva et al. 2010; McMillan and Schoenbohm 2020).

Finally, considering that the middle- to upper-tropospheric circulation is presently regulated by the Bolivian High anticyclone generating strong, north-northwesterly winds, and the surface uplift that the eastern Puna Plateau border experienced by ca. 15–6 Ma together with the establishment of the SALLJ, we propose that all these phenomena have worked together and influenced the development of an arid climate on the Puna Plateau since the late Miocene.

CONCLUSIONS

During the interval of 7.6–6.4 Ma, sediments were deposited in a sandy eolian to fluvio-eolian setting in the SAC basin, along the windward side of the eastern border of the Puna Plateau. These depositional environments developed over an irregular topography suggesting earlier surface uplift and exhumation of the previous units.

Our study, coupled with available information about late Miocene sandy eolian units along the Puna Plateau, indicates that the paleowind regime was ruled by northwesterly winds, with velocities of about 24–38 km/h

(reaching peaks of 55–75 km/h), which coincides with the present-day wind regime.

The uplift that the Puna Plateau–Eastern Cordillera experienced by the middle to late Miocene has contributed to the effectiveness of orographic barriers and the ensuing aridification towards the west. This also contributed to restricting the development of eolian systems towards the west, in the orogen's interior, by generating a topographic barrier for the migration and consequent accumulation of sand dunes on the windward sides of limiting ranges.

We conclude that the middle to upper level tropospheric circulation patterns on the Puna Plateau have remained constant over the last 8 Myr, and that the Bolivian High anticyclone has been regulating the wind regime since then.

ACKNOWLEDGMENTS

This study was financed by the Argentinian Research Projects: ANCyT, grant PICT 2016-N°1276 and the international cooperation program: SuRfAce processes, Tectonics and Georesources: the Andean foreland basin of Argentina (StRATEGy) CONICET, Ministry of Sciences, Research and Cultural Affairs, Germany. We thank J. Jaeggi for assistance during fieldwork and L. López-Steinmetz for earlier discussion on eolian sedimentation. We acknowledge the People of comunidades originarias by allowing access to the outcrops. Finally, we thank to L. Schoenbohm and M. Carr for their constructive reviews, and to A. Fildani and P. Burgess for the editorial handling of the manuscript. Our thanks to C. Laurin for editing the English text.

REFERENCES

Allmendinger, R.W., and Gubbels, T., 1996, Pure and simple shear plateau uplift, Altiplano–Puna, Argentina and Bolivia: Tectonophysics, v. 259, p. 1–13.

Allmendinger, R.W., Ramos, V.A., Jordan, T.E., Palma, M., and Isacks, B.L., 1983, Paleogeography and Andean structural geometry, northwestern Argentina: Tectonics, v. 2, p. 1–16.

Allmendinger, R.W., Jordan, T.E., Kay, S.M., and Isacks, B.L., 1997, The Evolution of the Altiplano–Puna Plateau of the Central Andes: Annual Review of Earth and Planetary Sciences, v. 25, p. 139–174.

Allmendinger, R.W., Cardozo, N., and Fischer, D.M., 2012, Structural Geology Algorithms: Vectors and Tensors: Cambridge University Press, 313 p.

Armijo, R., Lacassin, R., Coudurier-Curveur, A., and Carrizo, D., 2015, Coupled tectonic evolution of Andean orogeny and global climate: Earth-Science Reviews, v. 143, p. 1–35.

Arnosio, M., 2010, Evidencia textural y geoquímica de mezcla de magmas en el volcán Chimpa, Puna Salteña: Revista de la Asociación Geológica Argentina, v. 66, p. 253–270.

Arnosio, M., Marmol, V., and Becchio, R., 2005, Estratigrafía volcánica y evolución del centro volcánico El Morro (24° 17′ S 66° 15′ O) Puna Salteña: XVI Congreso Geológico Argentino, La Plata, Actas, p. 859–866.

Bagnold, R.A., 1941, The Physics of Blown Sand and Desert Dunes: London, Chapman and Hall, 102 p.

Bailey, J.E., Self, S., Wooller, L.K., and Mouginis-Mark, P.J., 2007, Discrimination of fluvial and eolian features on large ignimbrite sheets around La Pacana Caldera, Chile, using Landsat and SRTM-derived DEM: Remote Sensing of Environment, v. 108, p. 24–41.

Bianchi, A.R., Yáñez, C.E., and Acuña, L.R., 2005, Base de datos mensuales de precipitaciones del noroeste Argentino: Secretaría de Agricultura, Ganadería y Pesca de la Nación, Instituto Nacional de Tecnología Agripecuaria (INTA), Centro Regional Salta–Jujuy.

Blasco, G., Zappettini, E.O., and Hongn, F., 1996, Hoja Geológica 2566-I, San Antonio de los Cobres: Servicio Geológico Minero Argentino, Instituto de Geología y Recursos Minerales, Programa Nacional de Cartas Geológicas de la República Argentina, Provincias de Jujuy y de Salta, Boletín 217, 1:250,000.

Blott, S.J., and Pye, K., 2001, Gradistat: a grain size distribution and statistics package for the analysis of unconsolidated sediments: Earth Surface Processes and Landforms, v. 26, p. 1237–1248.

Bookhagen, B., and Strecker, M.R., 2008, Orographic barriers, high-resolution TRMM rainfall, and relief variations along the eastern Andes: Geophysical Research Letters, v. 35, L06403.

Bookhagen, B., and Strecker, M.R., 2012, Spatiotemporal trends in erosion rates across a pronounced rainfall gradient: examples from the southern Central Andes: Earth and Planetary Science Letters, v. 327–328, p. 97–110.

Bristow, C., and Mountney, N.P., 2013, Aeolian stratigraphy, *in* Shroder, J., editor in chief, Lancaster, N., Sherman, D.J., and Baas, A.C.W., eds., Treatise on Geomorphology: San Diego Academic Press, Aeolian Geomorphology, v. 11, p. 246–268.

Brookfield, M.E., 1977, The origin of bounding surfaces in ancient aeolian sandstones: Sedimentology, v. 24, p. 303–332.

Buitrago, L.G., Larran, M., Romano, R., Hurtado, R., Portal, M.R., Gonzalvez, M., Valdiviezo, M., Savio, A., and Gonzalez, P., 1999, El Clima de la Provincia de Jujuy, Segunda Edición: Cátedra de Climatología y Fenología Agrícola, Facultad de Ciencias Agrarias, Universidad Nacional de Jujuy, 39 p.

Carrapa, B., Adelmann, D., Hilley, G.E., Mortimer, E., Sobel, E.R., and Strecker, M.R., 2005, Oligocene range uplift and development of plateau morphology in the southern central Andes: Tectonics, v. 24, p. 1–19.

Carrapa, B., DeCelles, P.G., Reiners, P.W., Gehrels, G.E., and Sudo, M., 2009, Apatite triple dating and white mica $^{40}Ar/^{39}Ar$ thermochronology of syntectonic detritus in the Central Andes: a multiphase tectonothermal history: Geology, v. 37, p. 407–410.

Carrapa, B., Trimble, J.D., and Stockli, D.F., 2011, Patterns and timing of exhumation and deformation in the Eastern Cordillera of NW Argentina revealed by (U-Th)/He thermochronology: Tectonics, v. 30, p. 1–30.

Carrapa, B., Bywater-Reyes, S., DeCelles, P.G., Mortimer, E., and Gehrels, G.E., 2012, Late Eocene–Pliocene basin evolution in the Eastern Cordillera of northwestern Argentina (25°–26°S): regional implications for Andean orogenic wedge development: Basin Research, v. 23, p. 1–20.

Carrera, N., Muñoz, J.A., Sàbat, F., Mon, R., and Roca, E., 2006, The role of inversion tectonics in the structure of the Cordillera Oriental (NW Argentinean Andes): Journal of Structural Geology, v. 28, p. 1921–1932.

Coutand, I., Cobbold, P.R., de Urreiztieta, M., Gautier, P., Chauvin, A., Gapais, D., Rossello, E.A., and López-Gamundí, O., 2001, Style and history of Andean deformation, Puna Plateau, northwestern Argentina: Tectonics, v. 20, p. 210–234.

Coutand, I., Carrapa, B., Deeken, A., Schmitt, A.K., Sobel, E.R., and Strecker, M.R., 2006, Propagation of orographic barriers along an active range front: insights from sandstone petrography and detrital apatite fission–track thermochronology in the intramontane Angastaco basin, NWArgentina: Basin Research, v. 18, p. 1–18.

de Silva, S.L., Bailey, J.E., Mandt, K.E., and Viramonte, J.M., 2010, Yardangs in terrestrial ignimbrites: synergistic remote and field observations on Earth with applications to Mars: Planetary and Space Science, v. 58, p. 459–471.

DeCelles, P.G., Carrapa, B., and Gehrels, G.E., 2007, Detrital zircon U-Pb ages provide provenance and chronostratigraphic information from Eocene synorogenic deposits in northwestern Argentina: Geology, v. 35, p. 323–326.

DeCelles, P.G., Carrapa, B., Horton, B.K., and Gehrels, G.E., 2011, Cenozoic foreland basin system in the central Andes of northwestern Argentina: implications for Andean geodynamics and modes of deformation: Tectonics, v. 30, p. 1–30.

DeCelles, P.G., Carrapa, B., Horton, B.K., McNabb, J., Gehrels, G.E., and Boyd, J., 2015, The Miocene Arizaro Basin, central Andean hinterland: Response to partial lithosphere removal?, *in* DeCelles, P.G., Ducea, M.N., Carrapa, B., and Kapp, P.A., eds., Geodynamics of a Cordilleran Orogenic System: The Central Andes of Argentina and Northern Chile: Geological Society of America, Memoir 212, p. 359–386.

Deeken, A., Sobel, E.R., Coutand, I., Haschke, M., Riller, U., and Strecker, M.R., 2006, Development of the southern Eastern Cordillera, NW Argentina, constrained by apatite fission track thermochronology: from early Cretaceous extension to middle Miocene shortening: Tectonics, v. 26, p. 1–21.

del Papa, C., Hongn, F., Powell, J., Payrola, P., Do Campo, M., Strecker, M., Petrinovic, I., Smith, A., and Pereyra, R., 2013a, Middle Eocene–Oligocene broken-foreland evolution in the Andean Calchaquí Valley, NW Argentina: insights from stratigraphic, structural and provenance studies: Basin Research, v. 25, p. 574–593.

del Papa, C., Hong, F., Payrola, P., Powell, J., Deraco, V., and Herrera, C., 2013b, Relaciones estratigráficas de las Formaciones quebrada de los Colorados y Angastaco (Paleógeno–Neógeno), Valles Calchaquíes, Salta (Argentina): significado en el análisis de la cuenca del Grupo Payogastilla: Latin American Journal of Sedimentology and Basin Analysis, v. 20, p. 51–64.

del Papa, C.E., and Petrinovic, I.A., 2017, The development of Miocene extensional and short-lived basin in the Andean broken foreland: the Conglomerado Los Patos, Northwestern Argentina: Journal of South American Earth Sciences, v. 73, p. 191–201.

Dickinson, W.R., Beard, L.S., Brakenridge, G.R., Erjavec, J.L., Inman, K.F., Knepp, R.A., Lindberg, F.A., and Ryberg, P.T., 1983, Provenance of North American Phanerozoic sandstones in relation to tectonic settings: Geological Society of America, Bulletin, v. 94, p. 222–235.

DoCampo, M., Collo, G., and Nieto, F., 2013, Geothermobarometry of very low-grade metamorphic pelites of the Vendian–Early Cambrian Puncoviscana Formation (NW Argentina): European Journal of Mineralogy, v. 25, p. 429–451.

Ehlers, T.A., and Poulsen, C.J., 2009, Influence of Andean uplift on climate and paleoaltimetry estimates: Earth and Planetary Science Letters, v. 281, p. 238–248.

Escayola, M.P., van Staal, C.R., and Davis, W.J., 2011, The age and tectonic setting of the Puncoviscana Formation in northwestern Argentina: an accretionary complex related to Early Cambrian closure of the Puncoviscana Ocean and accretion of the Arequipa–Antofalla block: Journal of South American Earth Sciences, v. 32, p. 438–459.

Fiorella, R.P., Poulsen, C.J., Pillco Zolá, R.S., Barnes, J.B., Tabor, C.R., and Ehlers, T.A., 2015, Spatiotemporal variability of modern precipitation $\delta^{18}O$ in the central Andes and implications for paleoclimateand paleoaltimetry estimates: Journal of Geophysical Research, v. 120, p. 4630–4656.

Gaiero, D.M., 2007, Dust provenance in Antarctic ice during glacial periods: From where in southern South America?: Geophysical Research Letters, v. 34, p. 1–6.

Gaiero, D.M., Simonella, L., Gassó, S., Gili, S., Stein, A.F., Sosa, P., Becchio, R., Arce, J., and Marelli, H., 2013, Ground/satellite observations and atmospheric modeling of dust storms originating in the high Puna–Altiplano deserts (South America): implications for the interpretation of paleo-climatic archives: Journal of Geophysical Research: Atmospheres, v. 118, p. 1–15.

Garreaud, R.D., and Aceituno, P., 2007, Atmospheric circulation and climatic variability, *in* Veblen, T.T., Young, K.R., and Orme, A.R., eds., The Physical Geography of South America: Oxford University Press, p. 45–59.

Garreaud, R.D., Vuille, M., and Clement, A.C., 2003, The climate of the Altiplano: observed current conditions and mechanisms of past changes: Palaeogeography, Palaeoclimatology, Palaeoecology, v. 194, p. 5–22.

Garreaud, R.D., Molina, A., and Farias, M., 2010, Andean uplift, ocean cooling and Atacama hyperaridity: a climate modeling perspective: Earth and Planetary Science Letters, v. 292, p. 39–50.

Garzanti, E., Dinis, P., Vermeesch, P., Andò, S., Hahn, A., Huvi, J., Limonta, M., Padoan, M., Resentini, A., Rittner, M., and Vezzoli, G., 2018, Dynamic uplift, recycling, and climate control on the petrology of passive-margin sand (Angola): Sedimentary Geology, v. 375, p. 86–104.

Greene, L.L., 1995, Eolian landforms in the central Andes: implications for the long-term stability of atmospheric circulation [M.S. Thesis]: Ithaca, N.Y., Cornell University, 62 p.

Grier, M.E., Salfity, J.A., and Allmendinger, R.W., 1991, Andean reactivation of the Cretaceous Salta rift, northwestern Argentina: Journal of South American Earth Sciences, v. 4, p. 351–372.

Gutman, G.J., and Schwerdtfeger, W.S., 1965, The role of latent and sensible heat for the development of a high-pressure system over the subtropical Andes in the summer: Meteorologische Rundschau, v. 18, p. 69–75.

Harrington, H.J., and Leanza, A., 1957, Ordovician Trilobites of Argentina: Lawrence, University of Kansas Press, 276 p.

Hartley, A., 2003, Andean uplift and climate change: Geological Society of London, Journal, v. 160, p. 7–10.

Haschke, M., Deeken, A., Insel, N., Sobel, E., Grove, M., and Schmitt, A.K., 2005, Growth pattern of the Andean Puna plateau constrained by apatite fission track, apatite (U-Th)/He, K-feldespar $^{40}Ar/^{39}Ar$, and zircon U-Pb geochronology [Abstract]: 6th International Symposium on Andean Geodynamics, Barcelona, Extended Abstracts, p. 360–363.

Hongn, F.D., and Seggiaro, R.E., 2001, Hoja Geológica 2566-III, Cachi, Provincias de Salta y Catamarca: Buenos Aires, Servicio Geológico Minero Argentino, Boletín 248, p. 87, 1:250,000.

Houston, J., and Hartley, A.J., 2003, The central Andean west-slope rainshadow and its potential contribution to the origin of hyper-aridity in the Atacama desert: International Journal of Climatology, v. 23, p. 1453–1464.

Hunter, R.E., 1977, Basic types of stratification in small eolian dunes: Sedimentology, v. 24, p. 361–387.

Ingersoll, R.V., Bullard, T.F., Ford, R.L., Grimm, J.P., Pickle, J.D., and Sares, S.W., 1984, The effect of grain size on detrital modes: a test of the Gazzi–Dickinson point-counting method: Journal of Sedimentary Petrology, v. 54, p. 103–116.

Isacks, B.L., 1988, Uplift of the central Andean Plateau and bending of the Bolivian Orocline: Journal of Geophysical Research, v. 93, p. 3211–3231.

Kley, J., and Monaldi, C.R., 2002, Tectonic inversion in the Santa Barbara System of the central Andean foreland thrust belt, northwestern Argentina: Tectonics, v. 21, p. 1–18.

Kocurek, G., 1988, First-order and super bounding surfaces in eolian sequences: bounding surfaces revisited: Sedimentary Geology, v. 56, p. 193–206.

Kocurek, G., 1991, Interpretation of ancient eolian sand dunes: Annual Review of Earth and Planetary Sciences, v. 19, p. 43–75.

Kocurek, G., and Nielson, J., 1986, Conditions favourable for the formation of warm-climate aeolian sand sheets: Sedimentology, v. 33, p. 795–816.

Kraemer, B., Adelmann, D., Alten, M., Schnurr, W., Erpenstein, K., Kiefer, E., Van Den Bogaard, P., and Görler, K., 1999, Incorporation of the Paleogene foreland into the Neogene Puna plateau: the Salar de Antofalla area, NW Argentina: Journal of South American Earth Sciences, v. 12, p. 157–182.

Lamb, S., and Davis, P., 2003, Cenozoic climate change as a possible cause for the rise of the Andes: Nature, v. 425, p. 792–797.

Langford, R.P., and Chan, M.A., 1989, Fluvial–aeolian interactions: Part II, ancient systems: Sedimentology, v. 36, p. 1037–1051.

Ledesma, J., del Papa, C., and Payrola, P., 2019, Revisión de la estratigrafía Eocena–Pliocena de la cuenca intermontana de San Antonio de los Cobres, Puna Salteña, Argentina: Latin American Journal of Sedimentology and Basin Analysis, v. 26, p. 57–73.

Lenters, J.D., and Cook, K.H., 1997, On the origin of the Bolivian high and related circulation features of the South American climate: Journal of the Atmospheric Sciences, v. 54, p. 656–677.

Lenters, J.D., and Cook, K.H., 1999, Summertime precipitation variability over South America: role of the large-scale circulation: Monthly Weather Review, v. 127, p. 409–431.

López-Steinmetz, R.L., and López-Steinmetz, L.C., 2018, Paleo-eolian dynamics in the Andean Plateau: inferences from sedimentology of fossil and modern dunes: Journal of Sedimentary Research, v. 88, p. 129–147.

McKee, E.D., 1979, ed., A Study of Global Sand Seas: U.S. Geological Survey, Professional Paper 1052, 429 p.

McMillan, M., and Schoenbohm, L.M., 2020, Large-scale Cenozoic wind erosion in the Puna Plateau: the Salina del Fraile depression: Journal of Geophysical Research: Earth Surface, v. 125, p. 1–15.

Miall, A.D., 1996, The Geology of Fluvial Deposits: Sedimentary Facies, Basin Analysis, and Petroleum Geology: Springer-Verlag, 582 p.

Milana, J.P., and Kröhling, D.M., 2017, First data on volume and type of deflated sediment from Southern Puna Plateau and its role as source of the Chaco–Pampean loess: Quaternary International, v. 438, p. 126–140.

Mon, R., and Salfity, J.A., 1995, Tectonic evolution of the Andes of northern Argentina, *in Tankard,* SuárezA.J., Soruco, R., and Welsink, H.J., eds., Petroleum Basins of South America: American Association of Petroleum Geologists, Memoir 62, p. 269– 283.

Mulch, A., Uba, C.E., Strecker, M.R., Schoenberg, R., and Chamberlain, C.P., 2010, Late Miocene climate variability and surface elevation in the central Andes: Earth and Planetary Science Letters, v. 290, p. 173–182.

Norini, G., Baez, W., Becchio, R., Viramonte, J., Giordano, G., Arnosio, M., Pinton, A., and Groppelli, G., 2013, The Calama–Olacapato–El Toro fault system in the Puna Plateau, Central Andes: Geodynamic implications and stratovolcano emplacement: Tectonophysics, v. 608, p. 1280–1297.

Payrola, P., del Papa, C., Aramayo, A., Pingel, H., Hongn, F., Sobel, E.R., Zeilinger, G., Strecker, M.R., Zapata, S., Cottle, J., Salado Paz, N., and Glodny, J., 2020, Episodic out-of-sequence deformation promoted by Cenozoic fault reactivation in NW Argentina: Tectonophysics, v. 776, 228276.

Payrola, P., Zapata, S., Sobel, E.R., del Papa, C., Pingel, H., Glodny, J., and Ledesma, J., 2021, Exhumation and structural evolution of the high-elevation Malcante Range, Eastern Cordillera, NW Argentina: Journal of South American Earth Sciences, v. 105, p. 1–14.

Pearson, D.M., Kapp, P., Reiners, P.W., Gehrels, G.E., Ducea, M.N., Pullen, A., Otamendi, J.E., and Alonso, R.N., 2012, Major Miocene exhumation by fault-propagation folding within a metamorphosed, early Paleozoic thrust belt: northwestern Argentina: Tectonics, v. 31, TC4023.

Pearson, D.M., Kapp, P., DeCelles, P.G., Reiners, P.W., Gehrels, G.E., Ducea, M.N., and Pullen, A., 2013, Influence of pre-Andean crustal structure on Cenozoic thrust belt kinematics and shortening magnitude: Northwestern Argentina: Geosphere, v. 9, p. 1766–1782.

Petrinovic, I.A., Mitjavila, J., Viramonte, J., Martí, J., Becchio, R., Arnosio, M., and Colombo, F., 1999, Descripción geoquímica y geocronológica de secuencias volcánicas neógenas de Trasarco, en el extremo oriental de la Cadena Volcánica Transversal del Quevar (Noroeste de Argentina): Acta Geológica Hispánica, v. 34, p. 255–272.

Petrinovic, I.A., Riller, U., and Brod, J.A., 2005, The Negra Muerta Volcanic Complex, southern Central Andes: geochemical characteristics and magmatic evolution of an episodically active volcanic centre: Journal of Volcanology and Geothermal Research, v. 140, p. 295–320.

Pingel, H., Mulch, A., Alonso, R.N., Cottle, J., Hynek, S.A., Poletti, J., Rohrmann, A., Schmitt, A.K., Stockli, D.F., and Strecker, M.R., 2016, Surface uplift and convective rainfall along the southern Central Andes: Earth and Planetary Science Letters, v. 440, p. 33–42.

Pingel, H., Alonso, R.N., Altenberger, U., Cottle, J., and Strecker, M.R., 2019, Miocene to Quaternary basin evolution at the southeastern Andean Plateau (Puna) margin (ca. 24°S lat, Northwestern Argentina): Basin Research, p. 1–19.

Pingel, H., Strecker, M.R., Mulch, A., Alonso, R.N., Cottle, J., and Rohrmann, A., 2020, Late Cenozoic topographic evolution of the Eastern Cordillera and Puna Plateau margin in the southern Central Andes (NW Argentina): Earth and Planetary Science Letters, v. 535, p. 1–14.

Potter, P.E., and Pettijohn, F.J., 1977, Paleocurrents and Basin Analysis, 2nd Edition: Berlin, Springer-Verlag, 413 p.

Poulsen, C.J., Ehlers, T.A., and Insel, N., 2010, Onset of convective rainfall during gradual late Miocene rise of the central Andes: Science, v. 328, p. 490–493.

Pye, K., and Tsoar, H., 2009, Aeolian Sand and Sand Dunes: Berlin, Springer-Verlag 416 p.

Ramelow, J., Riller, U., Romer, R.L., and Oncken, O., 2006, Kinematic link between episodic trapdoor collapse of the Negra Muerta Caldera and motion on the Olacapato–El Toro Fault Zone, southern central Andes: International Journal of Earth Sciences, v. 95, p. 529–541.

Ramos, V.A., 1973, Estructura de los primeros contrafuertes de la Puna Saltojujeña y sus manifestaciones volcánicas asociadas: V Congreso Geológico Argentino, Actas, p. 159–202.

Reynolds, J.H., Galli, C.I., Hernández, R.M., Idleman, B.D., Kotila, J.M., Hilliard, R.V., and Naeser, C.W., 2000, Middle Miocene tectonic development of the Transition Zone, Salta Province, northwest Argentina: magnetic stratigraphy from the Metán Subgroup, Sierra de González: Geological Society of America, Bulletin, v. 112, p. 1736–1751.

Riller, U., and Hongn, F., 2003, Structural influence of Paleozoic discontinuities on Cretaceous to Quaternary tectonism in the Eastern Cordillera, NW-Argentina [Abstract]: European Geophysical Society, Geophysical Research Abstracts 5, no. 02303.

Riller, U., Petrinovic, I., Ramelow, J., Strecker, M., and Oncken, O., 2001, Late Cenozoic tectonism, collapse caldera and plateau formation in the Central Andes: Earth and Planetary Science Letters, v. 188, p. 299–311.

Rohrmann, A., Sachse, D., Mulch, A., Pingel, H., Tofelde, S., Alonso, R.N., and Strecker, M.R., 2016, Miocene orographic uplift forces rapid hydrological change in the southern central Andes: Scientific Reports, v. 6, p. 1–7.

Rubin, D.M., and Hunter, R.E., 1983, Reconstructing bedform assemblages from compound crossbedding, *in* Brookfield, M.E., and Ahlbrandt, T.S., eds., Eolian Sediments and Processes: Amsterdam, Elsevier, p. 407–427.

Salfity, J.A., and Marquillas, R.A., 1994, Tectonic and sedimentary evolution of the Cretaceous–Eocene Salta Group Basin, Argentina, *in* Salfity, J.A., ed., Cretaceous Tectonics of the Andes: Earth Evolution Sciences, Vieweg and Sohn, p. 266–315.

Schoenbohm, L.M., and Carrapa, B., 2015, Miocene–Pliocene shortening, extension, and mafic magmatism support small-scale lithospheric foundering in the central Andes, NW Argentina, *in* DeCelles, P.G., Ducea, M.N., Carrapa, B., and Kapp, P.A., eds., Geodynamics of a Cordilleran Orogenic System: The Central Andes of Argentina and Northern Chile: Geological Society of America, Memoir 212, p. 167–180.

Seggiaro, R.E., Becchio, R., Bercheñi V., and Ramallo, L., 2015, Hoja Geológica 2366-III Susques, provincias de Jujuy y Salta: Buenos Aires, Instituto de Geología y Recursos Minerales, Servicio Geológico Minero Argentino, Boletín 414, p. 103.

Seggiaro, R., Guzman, S., Pereyra, R., and Coppolecchia, M., 2016, Neotectónica y volcanismo monogenético Cuaternario sobre el segmento central del lineamiento Calama Olacapato Toro, NO Argentino: Revista de la Asociación Geológica Argentina, v. 73, p. 468–477.

Sobel, E.R., and Strecker, M.R., 2003, Uplift, exhumation and precipitation: tectonic and climatic control of late Cenozoic landscape evolution in the northern Sierras Pampeanas, Argentina: Basin Research, v. 15, p. 431–451.

Sobel, E.R., Hilley, G.E., and Strecker, M.R., 2003, Formation of internally drained contractional basins by aridity-limited bedrock incision: Journal of Geophysical Research, Solid Earth, v. 108, p. 1–23.

Starck, D., and Vergani, G., 1996, Desarrollo tectono-sedimentario del Cenozoico del sur de la Provincia de Salta, Argentina: XIII Congreso Geológico Argentino y III Congreso de Exploración de Hidrocarburos, Actas I, p. 433 – 452.

Strecker, M.R., Alonso, R.N., Bookhagen, B., Carrapa, B., Hilley, G.E., Sobel, E.R., and Trauth, M.H., 2007, Tectonics and climate of the southern central Andes: Annual Review of Earth and Planetary Sciences, v. 35, p. 747–787.

Tennekes, H., 1973, The logarithmic wind profile: Journal of the Atmospheric Sciences, v. 30, p. 234–238.

Tripaldi, A., 2012, La Formación Vallecito como ejemplo de sedimentación eólica Cenozoica de las cuencas andinas del Noroeste Argentino: paleoambientes y consideraciones estratigráficas y paleoclimáticas: Academia Nacional de Ciencias Exactas, Físicas y Naturales, Anales, v. 64, p. 55–71.

Tripaldi, A., and Limarino, C.O., 2005, Vallecito Formation (Miocene): the evolution of an eolian system in an Andean foreland basin (northwestern Argentina): Journal of South American Earth Sciences, v. 19, p. 343–357.

Turner, J.C., 1964, Descripción Geológica de la Hoja 7c, Nevado de Cachi, Provincia de Salta: Dirección Nacional de Geología y Minería, Buenos Aires, Boletín 99, 1:200,000.

Vandervoort, D.S., Jordan, T.E., Zeitler, P.K., and Alonso, R.N., 1995, Chronology of internal drainage development and uplift, southern Puna plateau, Argentine central Andes: Geology, v. 23, p. 145–148.

Vera, C., Baez, J., Douglas, M., Emmanuel, C.B., Marengo, J., Meitin, J., Nicolini, M., Nogues-Paegle, J., Peagle, J., Penalba, O., Salio, P., Saulo, C., Silva Dias, M.A., Silva Dias, P., and Zipser, E., 2006, The South American low-level jet experiment: American Meteorological Society, Bulletin, v. 87, p. 63–78.

Viramonte, J.G., Reynolds, J.H., del Papa, C., and Disalvo, A., 1994, The Corte Blanco garnetiferous tuff: a distinctive late Miocene marker bed in northwestern Argentina applied to magnetic polarity stratigraphy in the Río Yacones, Salta Province: Earth and Planetary Science Letters, v. 121, p. 519–531.

Virji, H., 1981, A preliminary study of summertime tropospheric circulation patterns over South America estimated from cloud winds: Monthly Weather Review. v. 109, p. 599–610.

von Kármán, T., 1935, Some aspects of the turbulence problem: Cambridge, MA, Fourth International Congress of Applied Mechanics, Proceedings, p. 54–91,

Vuille, M., 1999, Atmospheric circulation over the Bolivian Altiplano during dry and wet periods and extreme phases of the southern oscillation: International Journal of Climatology, v. 19, p. 1579–1600.

Zhou, R., Schoenbohm, L.M., Sobel, E.R., Carrapa, B., and Davis, D.W., 2016, Sedimentary record of regional deformation and dynamics of the thick-skinned southern Puna Plateau, central Andes (26–27°S): Earth and Planetary Science Letters, v. 433, p. 317–325.

Zuffa, G.G., 1985, Optical analyses of arenites: influence of methodology on compositional results, *in* Zuffa, G.G., ed., Provenance of Arenites: Reidel, Dordrecht, NATO ASI Series, v. 148, p. 165–189.

Zuffa, G.G., 1987, Unravelling hinterland and offshore palaeogeography from deep-water arenites, *in* Leggett, J.K., and Zuffa, G.G., eds., Marine Clastic Sedimentology: Concepts and Case Studies: London, Graham and Trotman, p. 39–61.

Received 2 February 2021; accepted 20 October 2021.